



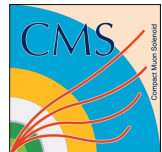
Universiteit Gent
Faculteit Wetenschappen
Vakgroep Fysica en Sterrenkunde

² No title yet

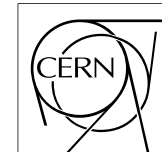
³ No sub-title neither, obviously...

⁴ Alexis Fagot

⁵



Thesis to obtain the degree of
Doctor of Philosophy in Physics
Academic years 2012-2017



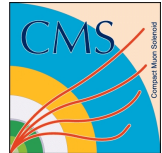


Universiteit Gent
Faculteit Wetenschappen
Vakgroep Fysica en Sterrenkunde

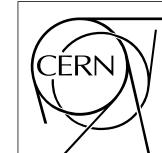
Promotoren: Dr. Michael Tytgat
Prof. Dr. Dirk Ryckbosch

Universiteit Gent
Faculteit Wetenschappen
Vakgroep Fysica en Sterrenkunde
Proeftuinstraat 86, B-9000 Gent, België
Tel.: +32 9 264.65.28
Fax.: +32 9 264.66.97

17



Thesis to obtain the degree of
Doctor of Philosophy in Physics
Academic years 2012-2017



18

Acknowledgements

19 Ici on remerciera tous les gens que j'ai pu croiser durant cette aventure et qui m'ont
20 permis de passer un bon moment

21

Gent, ici la super date de la mort qui tue de la fin d'écriture
22 *Alexis Fagot*

Table of Contents

23

24	Acknowledgements	i
25	Nederlandse samenvatting	xvii
26	English summary	xix
27	1 Introduction	1-1
28	1.1 A story of High Energy Physics	1-1
29	1.2 Organisation of this study	1-1
30	2 Investigating the TeV scale	2-1
31	2.1 The Standard Model of Particle Physics	2-1
32	2.2 The Large Hadron Collider and the Compact Muon Solenoid	2-1
33	2.3 Muon Phase-II Upgrade	2-1
34	3 Amplification processes in gaseous detectors	3-1
35	3.1 Signal formation	3-1
36	3.2 Gas transport parameters	3-1
37	4 Resistive Plate Chambers	4-1
38	4.1 Principle	4-1
39	4.2 Rate capability of Resistive Plate Chambers	4-1
40	4.3 High time resolution	4-1
41	4.4 Resistive Plate Chambers at CMS	4-1
42	4.4.1 Overview	4-1
43	4.4.2 The present RPC system	4-2
44	4.4.3 Pulse processing of CMS RPCs	4-3
45	5 Longevity studies and Consolidation of the present CMS RPC subsystem	5-1
46	5.1 Testing detectors under extreme conditions	5-1
47	5.1.1 The Gamma Irradiation Facilities	5-3
48	5.1.1.1 GIF	5-3
49	5.1.1.2 GIF++	5-5
50	5.2 Preliminary tests at GIF	5-8
51	5.2.1 Resistive Plate Chamber test setup	5-8

53	5.2.2	Data Acquisition	5-10
54	5.2.3	Geometrical acceptance of the setup layout to cosmic muons	5-10
55	5.2.3.1	Description of the simulation layout	5-11
56	5.2.3.2	Simulation procedure	5-13
57	5.2.3.3	Results	5-14
58	5.2.4	Photon flux at GIF	5-15
59	5.2.4.1	Expectations from simulations	5-15
60	5.2.4.2	Dose measurements	5-19
61	5.2.5	Results and discussions	5-20
62	5.3	Longevity tests at GIF++	5-21
63	5.3.1	Description of the Data Acquisition	5-25
64	5.3.2	RPC current, environmental and operation parameter monitoring	5-26
65	5.3.3	Measurement procedure	5-27
66	5.3.4	Longevity studies results	5-27
68	6	Investigation on high rate RPCs	6-1
69	6.1	Rate limitations and ageing of RPCs	6-1
70	6.1.1	Low resistivity electrodes	6-1
71	6.1.2	Low noise front-end electronics	6-1
72	6.2	Construction of prototypes	6-1
73	6.3	Results and discussions	6-1
74	7	Conclusions and outlooks	7-1
75	7.1	Conclusions	7-1
76	7.2	Outlooks	7-1
77	A	A data acquisition software for CAEN VME TDCs	A-1
78	A.1	GIF++ DAQ file tree	A-1
79	A.2	Description of the readout setup	A-2
80	A.3	Data read-out	A-5
81	A.3.1	V1190A TDCs	A-5
82	A.3.2	DataReader	A-8
83	A.3.3	V1718 USB Bridge	A-12
84	A.3.4	Configuration file	A-13
85	A.3.5	DAQ algorithm overview	A-16
86	A.4	Software export	A-16
87	B	Details on the online analysis package	B-1
88	B.1	Introduction	B-1
89	C	Structure of the hybrid simulation software	C-1
90	C.1	Introduction	C-1

List of Figures

91

92	2.1	Absorbed dose in the CMS cavern after an integrated luminosity of 3000 fb. R is the transverse distance from the beamline and Z is the distance along the beamline from the Interaction Point at Z=0.	2-2
93			
94			
95	2.2	A quadrant of the muon system, showing DTs (yellow), RPCs (light blue), and CSCs (green). The locations of new forward muon detectors for Phase-II are contained within the dashed box and indicated in red for GEM stations (ME0, GE1/1, and GE2/1) and dark blue for improved RPC (iRPC) stations (RE3/1 and RE4/1).	2-3
96			
97			
98			
99			
100	2.3	RMS of the multiple scattering displacement as a function of muon p_T for the proposed forward muon stations. All of the electromag- netic processes such as bremsstrahlung and magnetic field effect are included in the simulation.	2-4
101			
102			
103			
104	4.1	Signals from the RPC strips are shaped by the FEE described on Figure 4.1a. Output LVDS signals are then read-out by a TDC module connected to a computer or converted into NIM and sent to scalers. Figure 4.1b describes how these converted signals are put in coincidence with the trigger.	4-4
105			
106			
107			
108			
109	4.2	Description of the principle of a CFD. A comparison of threshold triggering (left) and constant fraction triggering (right) is shown in Figure 4.2a. Constant fraction triggering is obtained thanks to zero-crossing technique as explained in Figure 4.2b. The signal arriving at the input of the CFD is split into three components. A first one is delayed and connected to the inverting input of a first comparator. A second component is connected to the noninverting input of this first comparator. A third component is connected to the noninverting input of another comparator along with a thresh- old value connected to the inverting input. Finally, the output of both comparators is fed through an AND gate.	4-5
110			
111			
112			
113			
114			
115			
116			
117			
118			
119			
120	5.1	(5.1a) Extrapolation from 2016 data of single hit rate per unit area in the barrel region. (5.1b) Extrapolation from 2016 data of single hit rate per unit area in the endcap region.	5-2
121			
122			

123	5.2	Background Fluka simulation compared to 2016 Data at $L = 10^{34} \text{ cm}^{-2} \cdot \text{s}^{-1}$ in the fourth endcap disk region. A mismatch in between simulation and data can be observed. [To be understood.]	5-3
126	5.3	Layout of the test beam zone called X5c GIF at CERN. Photons from the radioactive source produce a sustained high rate of random hits over the whole area. The zone is surrounded by 8 m high and 80 cm thick concrete walls. Access is possible through three entry points. Two access doors for personnel and one large gate for material. A crane allows installation of heavy equipment in the area.	5-4
133	5.4	^{137}Cs decays by β^- emission to the ground state of ^{137}Ba (BR = 5.64%) and via the 662 keV isomeric level of ^{137}Ba (BR = 94.36%) whose half-life is 2.55 min.	5-5
136	5.5	Floor plan of the GIF++ facility. When the facility downstream of the GIF++ takes electron beam, a beam pipe is installed along the beam line (z-axis). The irradiator can be displaced laterally (its center moves from $x = 0.65$ m to 2.15 m), to increase the distance to the beam pipe.	5-6
141	5.6	Simulated unattenuated current of photons in the xz plane (Figure 5.6a) and yz plane (Figure 5.6b) through the source at $x = 0.65$ m and $y = 0$ m. With angular correction filters, the current of 662 keV photons is made uniform in xy planes.	5-7
145	5.7	Description of the RPC setup. Dimensions are given in mm. A tent containing RPCs is placed at 1720 mm from the source container. The source is situated in the center of the container. RE-4-2-BARC-161 chamber is 160 mm inside the tent. This way, the distance between the source and the chambers plan is 2060 mm. Figure 5.7a provides a side view of the setup in the xz plane while Figure 5.7b shows a top view in the yz plane.	5-8
152	5.8	RE-4-2-BARC-161 chamber is inside the tent as described in Figure 5.7. In the top right, the two scintillators used as trigger can be seen. This trigger system has an inclination of 10° relative to horizontal and is placed above half-partition B2 of the RPCs. PMT electronics are shielded thanks to lead blocks placed in order to protect them without stopping photons from going through the scintillators and the chamber.	5-9

159	5.9 Hit distributions over all 3 partitions of RE-4-2-BARC-161 chamber is showed on these plots. Top, middle and bottom figures respectively correspond to partitions A, B, and C. These plots show that some events still occur in other half-partitions than B2, which corresponds to strips 49 to 64, in front of which the trigger is placed, contributing to the inefficiency of detection of cosmic muons.	5-10
160		
161		
162		
163		
164		
165		
166		
167		
168		
169	5.10 Results are derived from data taken on half-partition B2 only. On the 18 th of June 2014, data has been taken on chamber RE-2-BARC-161 at building 904 (Prevessin Site) with cosmic muons providing us a reference efficiency plateau of $(97.54 \pm 0.15)\%$ represented by a black curve. A similar measurement has been done at GIF on the 21 st of July with the same chamber giving a plateau of $(78.52 \pm 0.94)\%$ represented by a red curve.	5-11
170		
171		
172		
173		
174		
175		
176	5.11 Representation of the layout used for the simulations of the test setup. The RPC is represented as a yellow trapezoid while the two scintillators as blue cuboids looking at the sky. A green plane corresponds to the muon generation plane within the simulation. Figure 5.7a shows a global view of the simulated setup. Figure 5.7b shows a zommed view that allows to see the 2 scintillators as well as the full RPC plane.	5-12
177		
178		
179		
180		
181		
182		
183	5.12 γ flux $F(D)$ is plot using values from table 5.1. As expected, the plot shows similar attenuation behaviours with increasing distance for each absorption factors.	5-15
184		
185		
186	5.13 Figure 5.13a shows the linear approximation fit done via formulae 5.7 on data from table 5.2. Figure 5.13b shows a comparison of this model with the simulated flux using a and b given in figure 5.13a in formulae 5.4 and the reference value $D_0 = 50\text{cm}$ and the associated flux for each absorption factor F_0^{ABS} from table 5.1	5-17
187		
188		
189		
190		
191		
192	5.14 Dose measurements has been done in a plane corresponding to the tents front side. This plan is 1900 mm away from the source. As explained in the first chapter, a lens-shaped lead filter provides a uniform photon flux in the vertical plan orthogonal to the beam direction. If the second line of measured fluxes is not taken into account because of lower values due to experimental equipments in the way between the source and the tent, the uniformity of the flux is well showed by the results.	5-19
193		
194		
195		
196		
197		
198		
199		
200	5.15	5-20

201	5.16 Evolution of the maximum efficiency for RE2 (5.16a) and RE4	
202	(5.16b) chambers with increasing extrapolated γ rate per unit area	
203	at working point. Both irradiated (blue) and non irradiated (red)	
204	chambers are shown.	5-22
205	5.17 Evolution of the working point for RE2 (5.17a) and RE4 (5.17b)	
206	with increasing extrapolated γ rate per unit area at working point.	
207	Both irradiated (blue) and non irradiated (red) chambers are shown. 5-23	
208	5.18 Evolution of the maximum efficiency at HL-LHC conditions, i.e.	
209	a background hit rate per unit area of 300 Hz/cm ² , with increasing	
210	integrated charge for RE2 (5.18a) and RE4 (5.18b) detectors. Both	
211	irradiated (blue) and non irradiated (red) chambers are shown. The	
212	integrated charge for non irradiated detectors is recorded during	
213	test beam periods and stays small with respect to the charge accu-	
214	mulated in irradiated chambers.	5-23
215	5.19 Comparison of the efficiency sigmoid before (triangles) and after	
216	(circles) irradiation for RE2 (5.19a) and RE4 (5.19b) detectors.	
217	Both irradiated (blue) and non irradiated (red) chambers are shown. 5-24	
218	5.20 Evolution of the Bakelite resistivity for RE2 (5.20a) and RE4 (5.20b)	
219	detectors. Both irradiated (blue) and non irradiated (red) chambers	
220	are shown.	5-24
221	5.21 Evolution of the noise rate per unit area for the irradiated chamber	
222	RE2-2-BARC-9 only.	5-25
223	A.1 (A.1a) View of the front panel of a V1190A TDC module [10].	
224	(A.1b) View of the front panel of a V1718 Bridge module [11].	
225	(A.1c) View of the front panel of a 6U 6021 VME crate [12]. . . A-4	
226	A.2 Module V1190A <i>Trigger Matching Mode</i> timing diagram [10]. . . A-6	
227	A.3 Structure of the ROOT output file generated by the DAQ. The 5	
228	branches (<code>EventNumber</code> , <code>number_of_hits</code> , <code>Quality_flag</code> , <code>TDC_channel</code>	
229	and <code>TDC_TimeStamp</code>) are visible on the left panel of the ROOT	
230	browser. On the right panel is visible the histogram corresponding	
231	to the variable <code>nHits</code> . In this specific example, there were approxi-	
232	mately 50k events recorded to measure the gamma irradiation rate	
233	on the detectors. Each event is stored as a single entry in the <code>TTree</code> . A-12	

List of Tables

235	5.1	Total photon flux ($E\gamma \leq 662$ keV) with statistical error predicted considering a ^{137}Cs activity of 740 GBq at different values of the distance D to the source along the x-axis of irradiation field [6]. . .	5-15
236	5.2	Correction factor c is computed thanks to formulae 5.5 taking as reference $D_0 = 50$ cm and the associated flux F_0^{ABS} for each ab- sorption factor available in table 5.1.	5-16
237	5.3	The data at D_0 in 1997 is taken from [6]. In a second step, using Equations 5.8 and 5.9, the flux at D can be estimated in 1997. Then, taking into account the attenuation of the source activity, the flux at D can be estimated at the time of the tests in GIF in 2014. Finally, assuming a sensitivity of the RPC to γ $s = 2 \cdot 10^{-3}$, an estimation of the hit rate per unit area is obtained.	5-18
238			
239			
240			
241			
242			
243			
244			
245			
246			

List of Acronyms

247

248

List of Acronyms

249

250

A

251

252

253 AFL

Almost Full Level

254

255

B

256

257

258 BARC

Bhabha Atomic Research Centre

259 BLT

Block Transfer

260 BR

Branching Ratio

261

262

C

263

264

265 CAEN

Costruzioni Apparecchiature Elettroniche Nucleari S.p.A.

266

267 CERN

European Organization for Nuclear Research

268 CFD

Constant Fraction Discriminator

269 CMS

Compact Muon Solenoid

270 CSC

Cathode Strip Chamber

271

272

D

273

274

275 DAQ

Data Acquisition

276 DCS

Detector Control Software

277 DQM

Data Quality Monitoring

278	DT	Drift Tube
279		
280		
281	F	
282		
283	FEE	Front-End Electronics
284	FEB	Front-End Board
285		
286		
287	G	
288		
289	GE-/-	Find a good description
290	GE1/1	Find a good description
291	GE2/1	Find a good description
292	GEANT	GEometry ANd Tracking - a series of software toolkit platforms developed by CERN
293		
294	GEM	Gas Electron Multiplier
295	GIF	Gamma Irradiation Facility
296	GIF++	new Gamma Irradiation Facility
297		
298		
299	H	
300		
301	HL-LHC	High Luminosity LHC
302	HV	High Voltage
303		
304		
305	I	
306		
307	iRPC	improved RPC
308	IRQ	Interrupt Request
309		
310		
311	L	
312		
313	LHC	Large Hadron Collider
314	LS1	First Long Shutdown
315	LS3	Third Long Shutdown

316	LV	Low Voltage
317	LVDS	Low-Voltage Differential Signaling
318		
319		
320	M	
321		
322	MC	Monte Carlo
323	MCNP	Monte Carlo N-Particle
324	ME-/-	Find good description
325	ME0	Find good description
326		
327		
328	N	
329		
330	NIM	Nuclear Instrumentation Module logic signals
331		
332		
333	P	
334		
335	PMT	PhotoMultiplier Tube
336		
337		
338	R	
339		
340	RE-/-	Find a good description
341	RE2/2	Find a good description
342	RE3/1	Find a good description
343	RE3/2	Find a good description
344	RE4/1	Find a good description
345	RE4/2	Find a good description
346	RE4/3	Find a good description
347	RMS	Root Mean Square
348	ROOT	a framework for data processing born at CERN
349	RPC	Resistive Plate Chamber
350		
351		
352	S	
353		
354	SPS	Super Proton Synchrotron

355

356

357 **T**

358

359 TDC

Time-to-Digital Converter

360

361

362 **W**

363

364 webDCS

Web Detector Control System

366

Nederlandse samenvatting –Summary in Dutch–

368 Le resume en Neerlandais (j'aurais peut-etre de apprendre la langue juste pour
369 ca...).

English summary

³⁷¹ Le meme résume mais en Anglais (on commencera par la hein!).

1

Introduction

³⁷² **1.1 A story of High Energy Physics**

³⁷³ **1.2 Organisation of this study**

397 to the beamline will have to withstand high irradiation, the radiation dose being of
398 the order of a few tens of Gy.

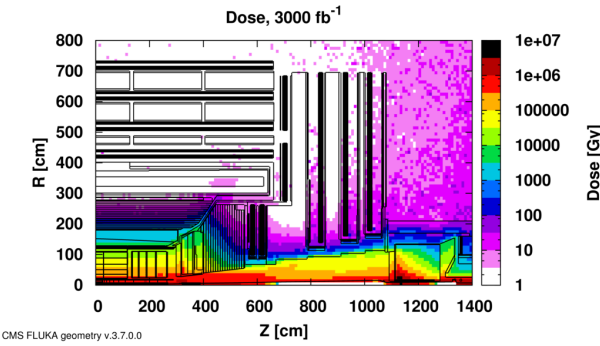


Figure 2.1: Absorbed dose in the CMS cavern after an integrated luminosity of 3000 fb. R is the transverse distance from the beamline and Z is the distance along the beamline from the Interaction Point at Z=0.

399 The measurement of small production cross-section and/or decay branching
400 ratio processes, such as the Higgs boson coupling to charge leptons or the $B_s \rightarrow$
401 $\mu^+ \mu^-$ decay, is of major interest and specific upgrades in the forward regions of
402 the detector will be required to maximize the physics acceptance on the largest
403 possible solid angle. To ensure proper trigger performance within the present cov-
404 erage, the muon system will be completed with new chambers. In figure 2.2 one
405 can see that the existing Cathode Strip Chambers (CSCs) will be completed by Gas
406 Electron Multipliers (GEMs) and Resistive Plate Chambers (RPCs) in the pseudo-
407 rapidity region $1.6 < |\eta| < 2.4$ to complete its redundancy as originally scheduled
408 in the CMS Technical Proposal [3].

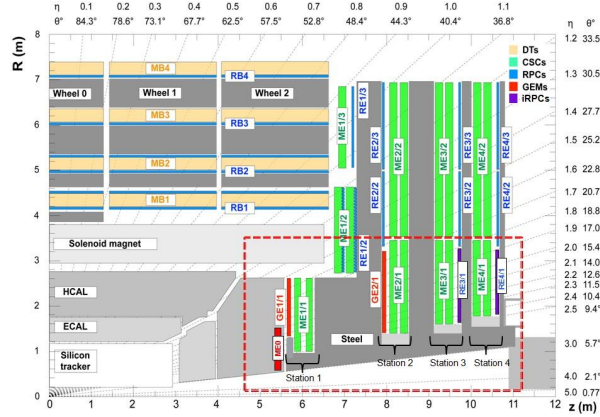


Figure 2.2: A quadrant of the muon system, showing DTs (yellow), RPCs (light blue), and CSCs (green). The locations of new forward muon detectors for Phase-II are contained within the dashed box and indicated in red for GEM stations (ME0, GE1/1, and GE2/1) and dark blue for improved RPC (iRPC) stations (RE3/1 and RE4/1).

409 RPCs are used by the CMS first level trigger for their good timing performances.
 410 Indeed, a very good bunch crossing identification can be obtained with the
 411 present CMS RPC system, given their fast response of the order of 1 ns. In order
 412 to contribute to the precision of muon momentum measurements, muon chambers
 413 should have a spatial resolution less or comparable to the contribution of multiple
 414 scattering [1]. Most of the plausible physics is covered only considering muons
 415 with $p_T < 100$ GeV thus, in order to match CMS requirements, a spatial resolu-
 416 tion of $\mathcal{O}(\text{few mm})$ the proposed new RPC stations, as shown by the simulation in
 417 figure 2.3. According to preliminary designs, RE3/1 and RE4/1 readout pitch will
 418 be comprised between 3 and 6 mm and 5 η -partitions could be considered.

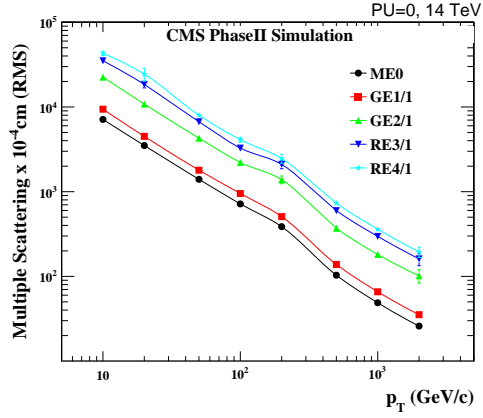


Figure 2.3: RMS of the multiple scattering displacement as a function of muon p_T for the proposed forward muon stations. All of the electromagnetic processes such as bremsstrahlung and magnetic field effect are included in the simulation.

3

419

420

421

Amplification processes in gaseous detectors

422 **3.1 Signal formation**

423 **3.2 Gas transport parameters**

4

424

425

Resistive Plate Chambers

426 4.1 Principle

427 4.2 Rate capability of Resistive Plate Chambers

428 4.3 High time resolution

429 4.4 Resistive Plate Chambers at CMS

430 4.4.1 Overview

431 The Resistive Plate Chambers (RPC) system, located in both barrel and endcap
432 regions, provides a fast, independent muon trigger with a looser p_T threshold over
433 a large portion of the pseudorapidity range ($|\eta| < 1.6$) [\[add reconstruction\]](#).

434

435 During High-Luminosity LHC (HL-LHC) operations the expected conditions
436 in terms of background and pile-up will make the identification and correct P_T as-
437 signment a challenge for the Muon system. The goal of RPC upgrade is to provide
438 additional hits to the Muon system with precise timing. All these informations will
439 be elaborated by the trigger system in a global way enhancing the performance of
440 the trigger in terms of efficiency and rate control. The RPC Upgrade is based
441 on two projects: an improved Link Board System and the extension of the RPC
442 coverage up to $|\eta| = 2.4$. [\[FIXME 2.4 or 2.5?\]](#)

443 The Link Board system, that will be described in section xxx, is responsible to
444 process, synchronize and zero-suppress the signals coming from the RPC front end
445 boards. The Link Board components have been produced between 2006 and 2007
446 and will be subjected to aging and failure in the long term. The upgraded Link
447 Board system will overcome the aging problems described in section xxx and will
448 allow for a more precise timing information to the RPC hits from 25 to 1 ns [ref
449 section xxx].

450 The extension of the RPC system up to $|\eta| = 2.1$ was already planned in the
451 CMS TDR [ref cmstdr] and staged because of budget limitations and expected
452 background rates higher than the rate capability of the present CMS RPCs in that
453 region. An extensive R&D program has been done in order to develop an improved
454 RPC that fulfills the CMS requirements. Two new RPC layers in the innermost ring
455 of stations 3 and 4 will be added with benefits to the neutron-induced background
456 reduction and efficiency improvement for both trigger and offline reconstruction.

457 4.4.2 The present RPC system

458 The RPC system is organized in 4 stations called RB1 to RB4 in the barrel region,
459 and RE1 to RE4 in the endcap region. The innermost barrel stations, RB1 and
460 RB2, are instrumented with 2 layers of RPCs facing the innermost (RB1in and
461 RB2in) and outermost (RB1out and RB2out) sides of the DT chambers. Every
462 chamber is then divided from the read-out point of view into 2 or 3 η partitions
463 called “rolls”. The RPC system consist of 480 barrel chambers and 576 endcap
464 chambers. Details on the geometry are discussed in the paper [ref to geo paper].

465 The CMS RPC chamber is a double-gap, operated in avalanche mode to ensure
466 reliable operation at high rates. Each RPC gap consists of two 2-mm-thick resistive
467 High-Pressure Laminate (HPL) plates separated by a 2-mm-thick gas gap. The
468 outer surface of the HPL plates is coated with a thin conductive graphite layer, and
469 a voltage is applied. The RPCs are operated with a 3-component, non-flammable
470 gas mixture consisting of 95.2% freon ($C_2H_2F_4$, known as R134a), 4.5% isobutane
471 ($i-C_4H_{10}$), and 0.3% sulphur hexafluoride (SF_6) with a relative humidity of 40% -
472 50%. Readout strips are aligned in η between the 2 gas gaps. [\[Add a sentence on
473 FEBs.\]](#)

474 The discriminated signals coming from the Front End boards feed via twisted
475 cables (10 to 20 m long) the Link Board System located in UXC on the balconies
476 around the detector. The Link System consist of the 1376 Link Boards (LBs)
477 and the 216 Control Boards (CBs), placed in 108 Link Boxes. The Link Box
478 is a custom crate (6U high) with 20 slots (for two CBs and eighteen LBs). The
479 Link Box contains custom backplane to which the cables from the chambers are
480 connected, as well as the cables providing the LBs and CBs power supply and the
481 cables for the RPC FEBs control with use of the I2C protocol (trough the CB). The

482 backplane itself contains only connectors (and no any other electronic devices).

483 The Link Board has 96 input channels (one channel corresponds to one RPC
484 strip). The input signals are the ~ 100 ns binary pulses which are synchronous to
485 the RPC hits, but not to the LHC clock (which drives the entire CMS electronics).
486 Thus the first step of the FEB signals processing is synchronization, i.e. assign-
487 ment of the signals to the BXes (25 ns periods). Then the data are compressed with
488 a simple zero-suppressing algorithm (the input channels are grouped into 8 bit par-
489 titions, only the partitions with at least one nonzero bit are selected for each BX).
490 Next, the non-empty partitions are time-multiplexed i.e. if there are more than one
491 such partition in a given BX, they are sent one-by-one in consecutive BXes. The
492 data from 3 neighbouring LBs are concentrated by the middle LB which contains
493 the optical transmitter for sending them to the USC over a fiber at 1.6 Gbps.

494 The Control Boards provide the communication of the control software with
495 the LBs via the FEC/CCU system. The CBs are connected into token rings, each
496 ring consists of 12 CBs of one detector tower and a FEC mezzanine board placed
497 on the CCS board located in the VME crate in the USC. In total, there are 18 rings
498 in the entire Link System. The CBs also perform automatic reloading of the LB's
499 firmware which is needed in order to avoid accumulation of the radiation induced
500 SEUs in the LBs firmware.

501 Both LBs and CB are based on the Xilinx Spartan III FPGAs, the CB addition-
502 ally contains radiation-tolerant (FLASH based) FPGA Actel ProAsicPlus.

503 The High Voltage power system is located in USC, not exposed to radiation and
504 easily accessible for any reparation. A single HV channel powers 2 RPC chambers
505 both in the barrel and endcap regions. The Low Voltage boards are located in UXC
506 on the balconies and provide the voltage to the front end electronics.

507 **4.4.3 Pulse processing of CMS RPCs**

508 Signals induced by cosmic particle in the RPC strips are shaped by standard CMS
509 RPC Front-End Electronics (FEE) following the scheme of Figure 4.1. On a first
510 stage, analogic signals are amplified and then sent to the Constant Fraction Dis-
511 criminator (CFD) described in Figure 4.2. At the end of the chain, 100 ns long
512 pulses are sent in the LVDS output. These output signal are sent on one side to a
513 V1190A Time-to-Digital Converter (TDC) module from CAEN and on the other
514 to an OR module to count the number of detected signals. Trigger and hit coïnci-
515 dences are monitored using scalers. The TDC is used to store the data into ROOT
516 files. These files are thus analysed to understand the detectors performance.

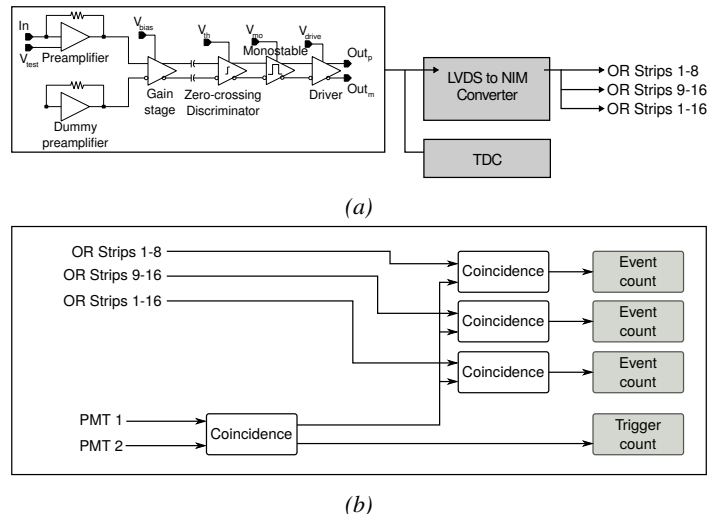


Figure 4.1: Signals from the RPC strips are shaped by the FEE described on Figure 4.1a. Output LVDS signals are then read-out by a TDC module connected to a computer or converted into NIM and sent to scalers. Figure 4.1b describes how these converted signals are put in coincidence with the trigger.

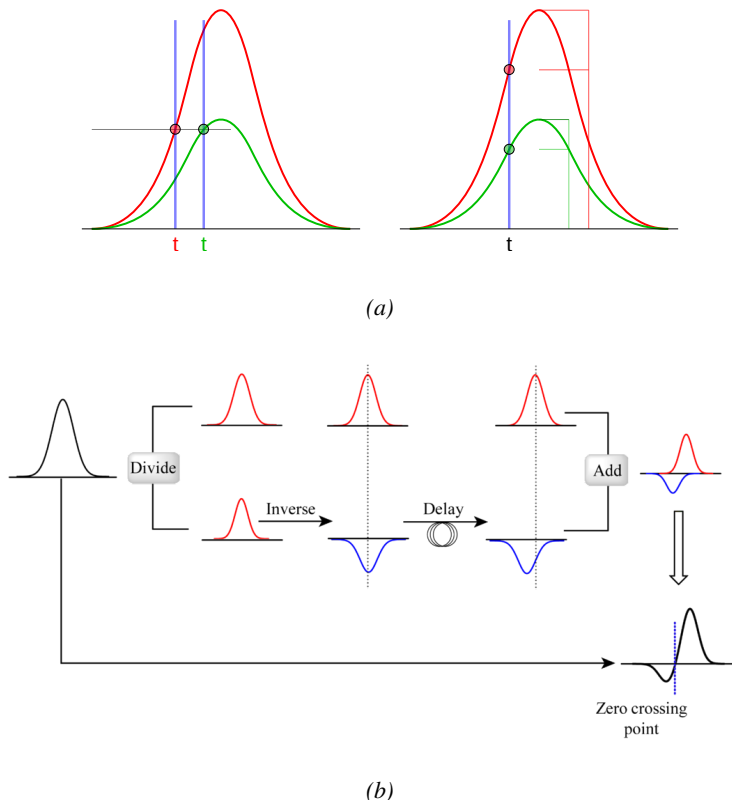


Figure 4.2: Description of the principle of a CFD. A comparison of threshold triggering (left) and constant fraction triggering (right) is shown in Figure 4.2a. Constant fraction triggering is obtained thanks to zero-crossing technique as explained in Figure 4.2b. The signal arriving at the input of the CFD is split into three components. A first one is delayed and connected to the inverting input of a first comparator. A second component is connected to the noninverting input of this first comparator. A third component is connected to the noninverting input of another comparator along with a threshold value connected to the inverting input. Finally, the output of both comparators is fed through an AND gate.

5

517

518 Longevity studies and Consolidation of 519 the present CMS RPC subsystem

520 **5.1 Testing detectors under extreme conditions**

521 The upgrade from LHC to HL-LHC will increase the peak luminosity from 10^{34}
522 $\text{cm}^{-2} \text{s}^{-1}$ to reach $5 \times 10^{34} \text{ cm}^{-2} \text{s}^{-1}$, increasing in the same way the total ex-
523 pected background to which the RPC system will be subjected to. Composed of
524 low energy gammas and neutrons from p - p collisions, low momentum primary
525 and secondary muons, puch-through hadrons from calorimeters, and particles pro-
526 duced in the interaction of the beams with collimators, the background will mostly
527 affect the regions of CMS that are the closest to the beam line, i.e. the RPC detec-
528 tors located in the endcaps. [To update.]

529

530 The 2016 data allowed to study the values of the background rate in all RPC
531 system. In Figure 5.1, the distribution of the chamber background hit rate per unit
532 area is shown at a luminosity of $5 \times 10^{34} \text{ cm}^{-2} \cdot \text{s}^{-1}$ linearly extrapolating from
533 data collected in 2016 [ref mentioning the linear dependency of rate vs lumi]. The
534 maximum rate per unit area at HL-LHC conditions is expected to be of the or-
535 der of 600 Hz/cm^2 (including a safety factor 3). Nevertheless, Fluka simulations
536 have conducted in order to understand the background at HL-LHC conditions. The
537 comparison to the data has shown, in Figure 5.2, a discrepancy of a factor 2 even
538 though the order of magnitude is consistent. [Understand mismatch.]

539

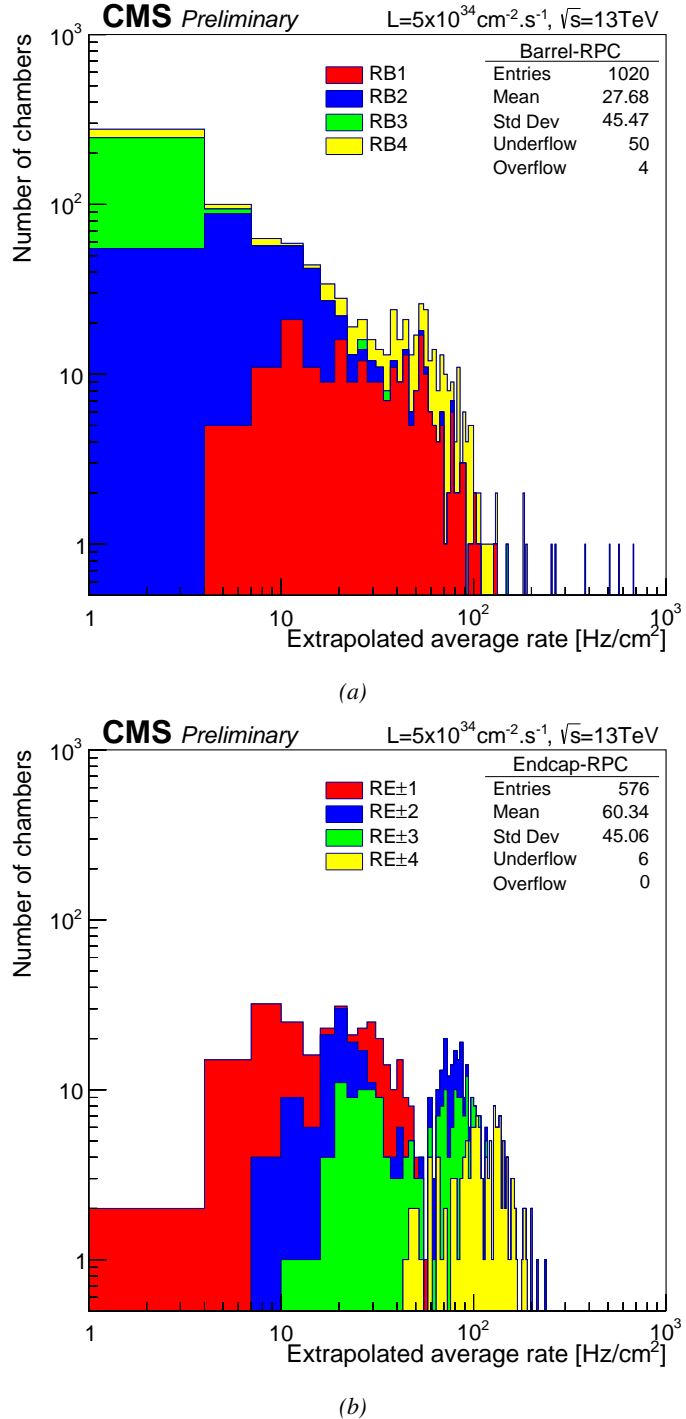


Figure 5.1: (5.1a) Extrapolation from 2016 data of single hit rate per unit area in the barrel region. (5.1b) Extrapolation from 2016 data of single hit rate per unit area in the endcap region.

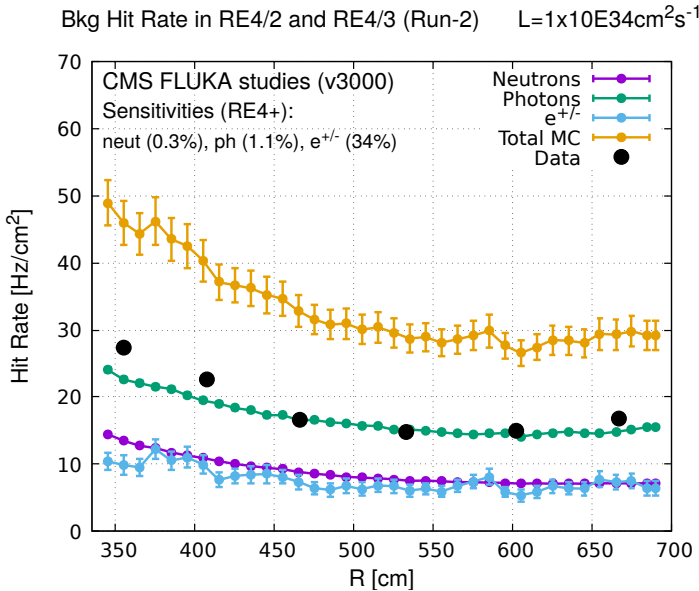


Figure 5.2: Background Fluka simulation compared to 2016 Data at $L = 10^{34} \text{ cm}^{-2} \cdot \text{s}^{-1}$ in the fourth endcap disk region. A mismatch in between simulation and data can be observed. [\[To be understood.\]](#)

540 In the past, extensive long-term tests were carried out at several gamma and
 541 neutron facilities certifying the detector performance. Both full size and small
 542 prototype RPCs have been irradiated with photons up to an integrated charge of
 543 $\sim 0.05 \text{ C}/\text{cm}^2$ and $\sim 0.4 \text{ C}/\text{cm}^2$, respectively [4, 5]. During Run-I, the RPC sys-
 544 tem provided stable operation and excellent performance and did not show any
 545 aging effects for integrated charge of the order of $0.01 \text{ C}/\text{cm}^2$. Projections on cur-
 546 rents from 2016 Data, has allowed to determine that the total integrated charge, by
 547 the end of HL-LHC, would be of the order of $1 \text{ C}/\text{cm}^2$ (including a safety factor
 548 3). [\[Corresponding figure needed.\]](#)

549

550 5.1.1 The Gamma Irradiation Facilities

551 5.1.1.1 GIF

552 Located in the SPS West Area at the downstream end of the X5 test beam, the
 553 Gamma Irradiation Facility (GIF) was a test area in which particle detectors were
 554 exposed to a particle beam in presence of an adjustable gamma background [6].
 555 Its goal was to reproduce background conditions these detectors would suffer in
 556 their operating environment at LHC. GIF layout is shown in Figure 5.3. Gamma

557 photons are produced by a strong ^{137}Cs source installed in the upstream part of the
 558 zone inside a lead container. The source container includes a collimator, designed
 559 to irradiate a $6 \times 6 \text{ m}^2$ area at 5 m maximum to the source. A thin lens-shaped lead
 560 filter helps providing with a uniform outgoing flux in a vertical plane, orthogonal
 561 to the beam direction. The principal collimator hole provides a pyramidal aperture
 562 of $74^\circ \times 74^\circ$ solid angle and provides a photon flux in a pyramidal volume along
 563 the beam axis. The photon rate is controled by further lead filters allowing the
 564 maximum rate to be limited and to vary within a range of four orders of magni-
 565 tude. Particle detectors under test are then placed within the pyramidal volume
 566 in front of the source, perpendicularly to the beam line in order to profit from the
 567 homogeneous photon flux. Adjusting the background flux of photons can then be
 568 done by using the filters and choosing the position of the detectors with respect to
 569 the source.

570

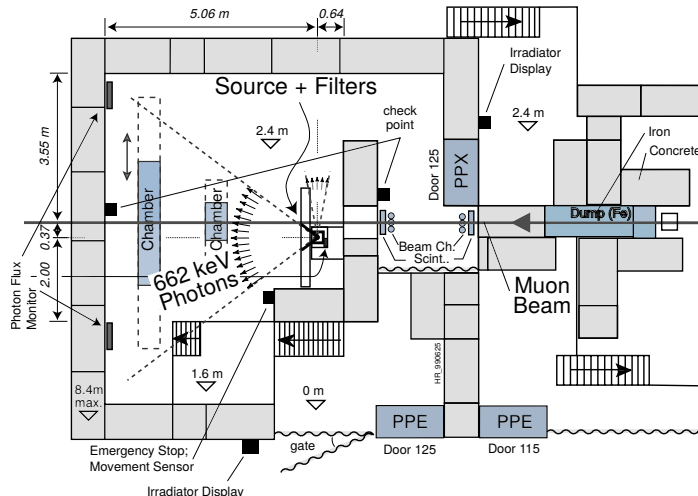


Figure 5.3: Layout of the test beam zone called X5c GIF at CERN. Photons from the radioactive source produce a sustained high rate of random hits over the whole area. The zone is surrounded by 8 m high and 80 cm thick concrete walls. Access is possible through three entry points. Two access doors for personnel and one large gate for material. A crane allows installation of heavy equipment in the area.

571 As described on Figure 5.4, the ^{137}Cs source emits a 662 keV photon in 85%
 572 of the decays. An activity of 740 GBq was measured on the 5th March 1997. To
 573 estimate the strength of the flux in 2014, it is necessary to consider the nuclear
 574 decay through time assiciated to the Cesium source whose half-life is well known
 575 ($t_{1/2} = (30.05 \pm 0.08) \text{ y}$). The GIF tests where done in between the 20th and the
 576 31st of August 2014, i.e. at a time $t = (17.47 \pm 0.02) \text{ y}$ resulting in an attenuation

577 of the activity from 740 GBq in 1997 to 494 GBq in 2014.

578

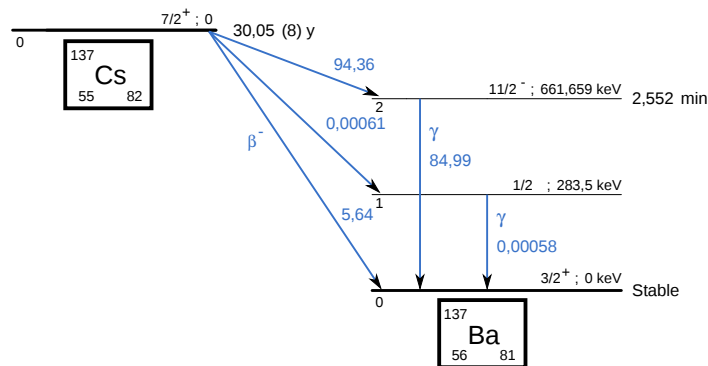


Figure 5.4: ^{137}Cs decays by β^- emission to the ground state of ^{137}Ba (BR = 5.64%) and via the 662 keV isomeric level of ^{137}Ba (BR = 94.36%) whose half-life is 2.55 min.

579 5.1.1.2 GIF++

580 The new Gamma Irradiation Facility (GIF++), located in the SPS North Area at
 581 the downstream end of the H4 test beam, has replaced its predecessor during LS1
 582 and has been operational since spring 2015 [7]. Like GIF, GIF++ features a ^{137}Cs
 583 source of 662 keV gamma photons, their fluence being controlled with a set of
 584 filters of various attenuation factors. The source provides two separated large irra-
 585 diation areas for testing several full-size muon detectors with continuous homo-
 586 geneous irradiation, as presented in Figure 5.5.

587

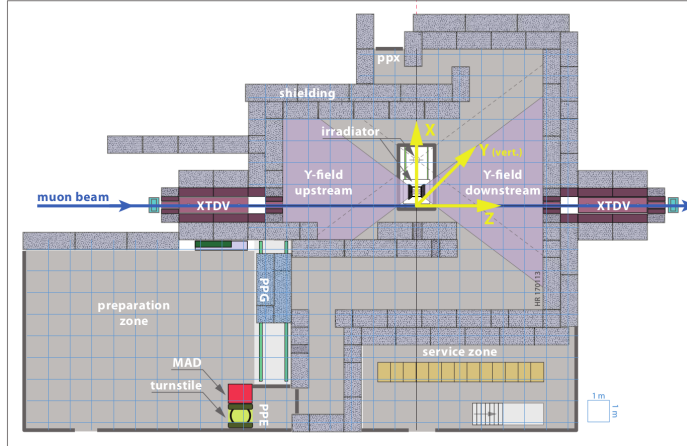


Figure 5.5: Floor plan of the GIF++ facility. When the facility downstream of the GIF++ takes electron beam, a beam pipe is installed along the beam line (z -axis). The irradiator can be displaced laterally (its center moves from $x = 0.65$ m to 2.15 m), to increase the distance to the beam pipe.

588 The source activity was measured to be about 13.5 TBq in March 2016. The
 589 photon flux being far greater than HL-LHC expectations, GIF++ provides an ex-
 590 cellent facility for accelerated aging tests of muon detectors.

591

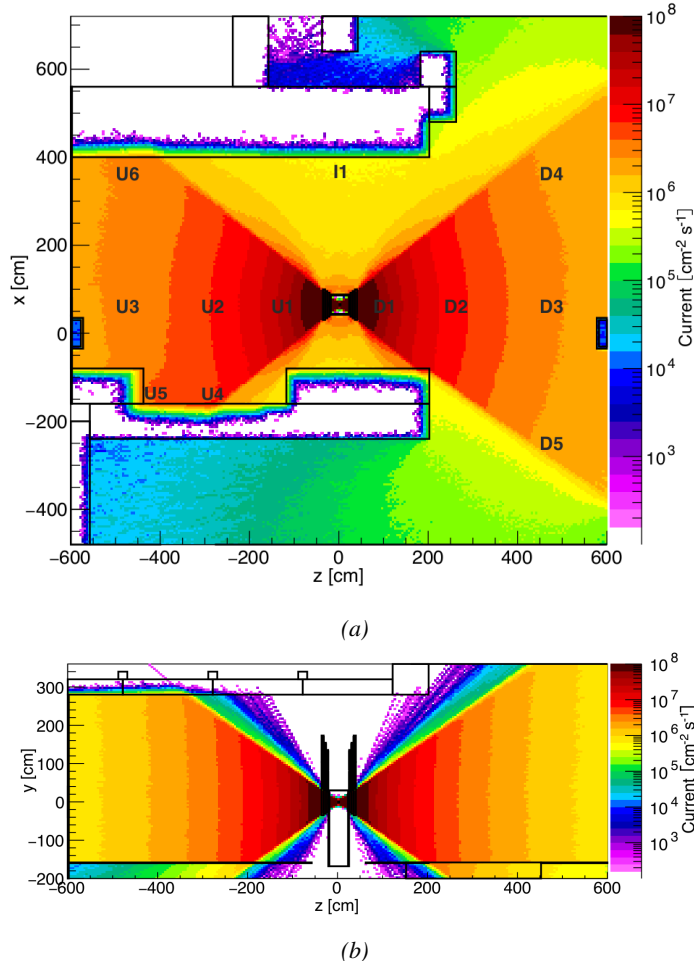


Figure 5.6: Simulated unattenuated current of photons in the xz plane (Figure 5.6a) and yz plane (Figure 5.6b) through the source at $x = 0.65$ m and $y = 0$ m. With angular correction filters, the current of 662 keV photons is made uniform in xy planes.

592 The source is situated in the muon beam line with the muon beam being avail-
 593 able a few times a year. The H4 beam, composed of muons with a momentum of
 594 about 150 GeV/c, passes through the GIF++ zone and is used to study the per-
 595 formance of the detectors. Its flux is of 104 particles/s/cm² focused in an area
 596 similar to 10×10 cm². Therefore, with properly adjusted filters, one can imitate
 597 the HL-LHC background and study the performance of muon detectors with their
 598 trigger/readout electronics in HL-LHC environment.
 599

5.2 Preliminary tests at GIF

5.2.1 Resistive Plate Chamber test setup

During summer 2014, preliminary tests have been conducted in the GIF area on a newly produced RE4/2 chamber labelled RE-4-2-BARC-161. This chamber has been placed into a trolley covered with a tent. The position of the RPC inside the tent and of the tent related to the source is described in Figure 5.7. To test this CMS RPC, three different absorber settings were used. First of all, measurements were done with fully opened source. Then, to complete this preliminary study, the gamma flux has been attenuated from a factor 2 and a factor 5. The expected gamma flux at the level of our detector will be discussed in subsection 5.2.4.

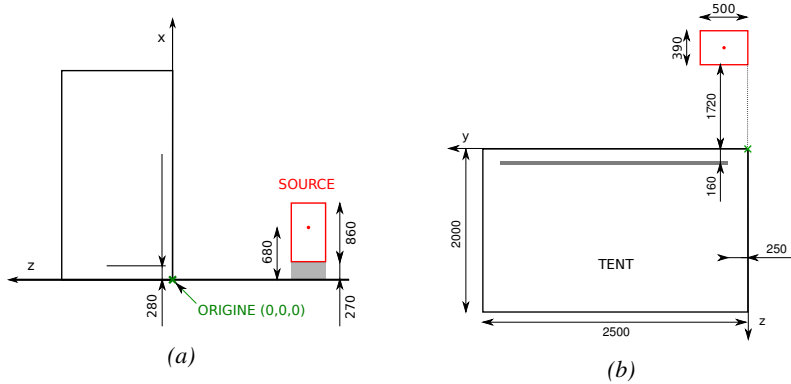


Figure 5.7: Description of the RPC setup. Dimensions are given in mm. A tent containing RPCs is placed at 1720 mm from the source container. The source is situated in the center of the container. RE-4-2-BARC-161 chamber is 160 mm inside the tent. This way, the distance between the source and the chambers plan is 2060 mm. Figure 5.7a provides a side view of the setup in the xz plane while Figure 5.7b shows a top view in the yz plane.



Figure 5.8: RE-4-2-BARC-161 chamber is inside the tent as described in Figure 5.7. In the top right, the two scintillators used as trigger can be seen. This trigger system has an inclination of 10° relative to horizontal and is placed above half-partition B2 of the RPCs. PMT electronics are shielded thanks to lead blocks placed in order to protect them without stopping photons from going through the scintillators and the chamber.

610 At the time of the tests, the beam not being operational anymore, a trigger
611 composed of 2 plastic scintillators has been placed in front of the setup with an
612 inclination of 10 deg with respect to the detector plane in order to look at cosmic
613 muons. Using this particular trigger layout, shown on Figure 5.8, leads to a cosmic
614 muon hit distribution into the chamber similar to the one in Figure 5.9. Measured
615 without gamma irradiation, two peaks can be seen on the profil of partition B, cen-
616 tered on strips 52 and 59. Section 5.2.3 will help us understand that these two peaks
617 are due respectively to forward and backward coming cosmic particles where for-
618 ward coming particles are first detected by the scintillators and then the RPC while
619 the backward coming muons are first detected in the RPC.

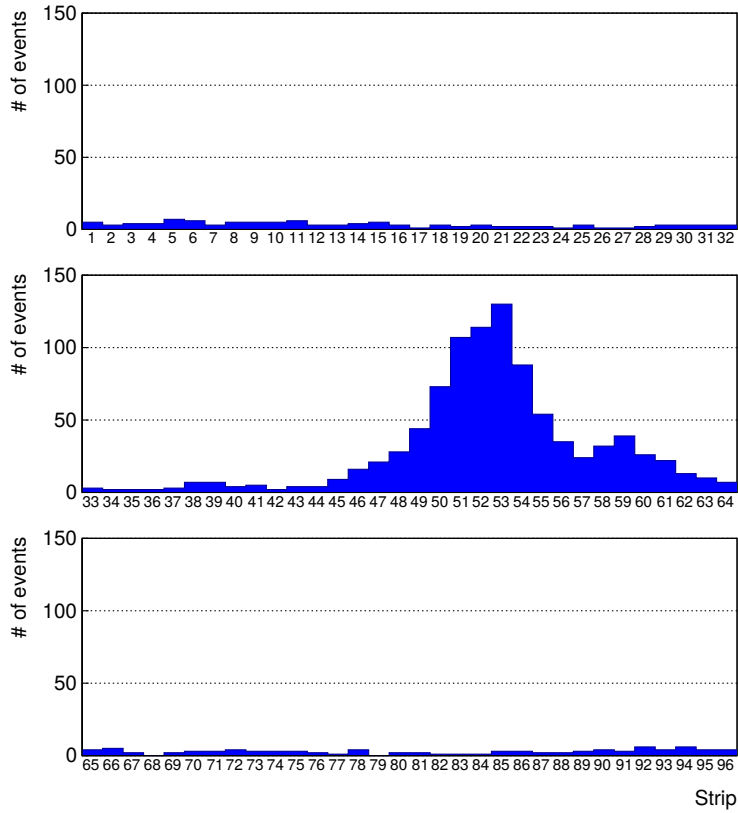


Figure 5.9: Hit distributions over all 3 partitions of RE-4-2-BARC-161 chamber is showed on these plots. Top, middle and bottom figures respectively correspond to partitions A, B, and C. These plots show that some events still occur in other half-partitions than B2, which corresponds to strips 49 to 64, in front of which the trigger is placed, contributing to the inefficiency of detection of cosmic muons. In the case of partitions A and C, the very low amount of data can be interpreted as noise. On the other hand, it is clear that a little portion of muons reach the half-partition B1, corresponding to strips 33 to 48.

620 5.2.2 Data Acquisition

621 5.2.3 Geometrical acceptance of the setup layout to cosmic muons

622 In order to profit from a constant gamma irradiation, the detectors inside of the GIF
 623 bunker need to be placed in a plane orthogonal to the beam line. The muon beam
 624 that used to be available was meant to test the performance of detectors under test.
 625 This beam not being active anymore, another solution to test detector performance
 626 had to be used. Thus, it has been decided to use cosmic muons detected through

627 a telescope composed of two scintillators. Lead blocks were used as shielding to
 628 protect the photomultipliers from gammas as can be seen from Figure 5.8.

629 An inclination has been given to the cosmic telescope to maximize the muon
 630 flux. A good compromise had to be found between good enough muon flux and
 631 narrow enough hit distribution to be sure to contain all the events into only one half
 632 partitions as required from the limited available readout hardware. Nevertheless,
 633 a consequence of the misplaced trigger, that can be seen as a loss of events in
 634 half-partition B1 in Figure 5.9, is an inefficiency. Nevertheless, the inefficiency
 635 of approximately 20 % highlighted in Figure 5.10 by comparing the performance
 636 of chamber BARC-161 in 904 and at GIF without irradiation seems too important
 637 to be explained only by the geometrical acceptance of the setup itself. Simulations
 638 have been conducted to show how the setup brings inefficiency.

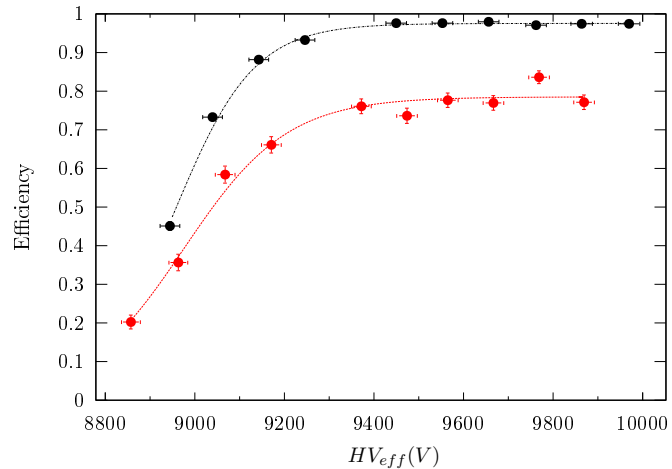


Figure 5.10: Results are derived from data taken on half-partition B2 only. On the 18th of June 2014, data has been taken on chamber RE-2-BARC-161 at building 904 (Prevessin Site) with cosmic muons providing us a reference efficiency plateau of $(97.54 \pm 0.15)\%$ represented by a black curve. A similar measurement has been done at GIF on the 21st of July with the same chamber giving a plateau of $(78.52 \pm 0.94)\%$ represented by a red curve.

639 5.2.3.1 Description of the simulation layout

640 The layout of GIF setup has been reproduced and incorporated into a Monte Carlo
 641 (MC) simulation to study the influence of the disposition of the telescope on the
 642 final distribution measured by the RPC. A 3D view of the simulated layout is given
 643 into Figure 5.11. Muons are generated randomly in a horizontal plane located at a
 644 height corresponding to the lowest point of the PMTs. This way, the needed size
 645 of the plane in order to simulate events happening at very big azimuthal angles (i.e.

646 $\theta \approx \pi$) can be kept relatively small. The muon flux is designed to follow the usual
 647 $\cos^2\theta$ distribution for cosmic particle. The goal of the simulation is to look at
 648 muons that pass through the muon telescope composed of the two scintillators and
 649 define their distribution onto the RPC plane. During the reconstruction, the RPC
 650 plane is then divided into its strips and each muon track is assigned to a strip.

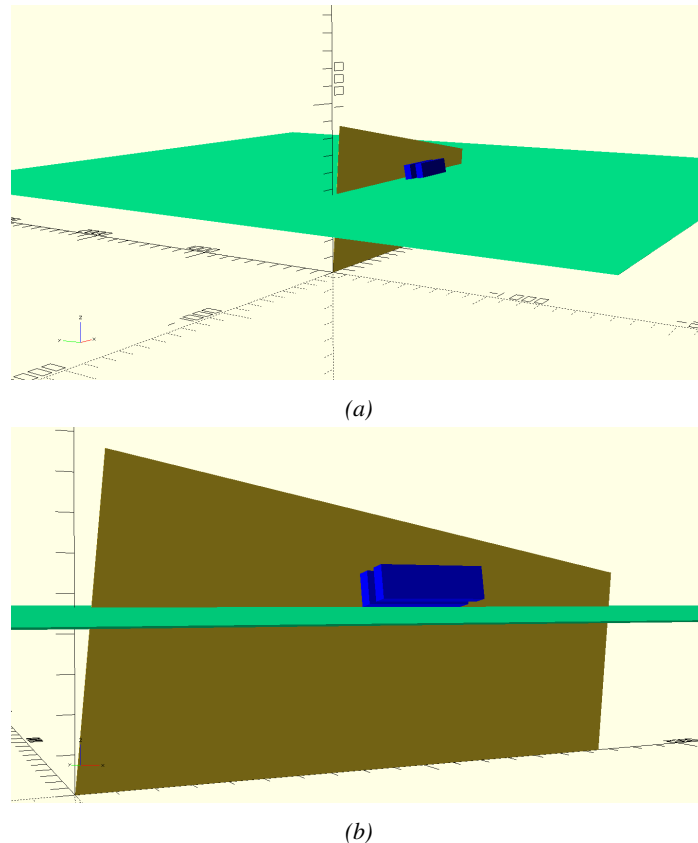


Figure 5.11: Representation of the layout used for the simulations of the test setup. The RPC is represented as a yellow trapezoid while the two scintillators as blue cuboids looking at the sky. A green plane corresponds to the muon generation plane within the simulation. Figure 5.7a shows a global view of the simulated setup. Figure 5.7b shows a zoomed view that allows to see the 2 scintillators as well as the full RPC plane.

651 In order to further refine the quality of the simulation and understand deeper
 652 the results the dependance of the distribution has been studied for a range of tele-
 653 scope inclinations. Moreover, the threshold applied on the PMT signals has been
 654 included into the simulation in the form of a cut. In the approximation of uni-
 655 form scintillators, it has been considered that the threshold can be understood as

656 the minimum distance particles need to travel through the scintillating material to
657 give a strong enough signal. Particles that travel a distance smaller than the set
658 "threshold" are thus not detected by the telescope and cannot trigger the data tak-
659 ing. Finally, the FEE threshold also has been considered in a similar way. The
660 mean momentum of horizontal cosmic rays is higher than those of vertical ones
661 but the stopping power of matter for momenta ranging from 1 GeV to 1 TeV stays
662 comparable. It is then possible to assume that the mean number of primary e^-/ion
663 pairs per unit length will stay similar and thus, depending on the applied discrimi-
664 nator threshold, muons with the shortest path through the gas volume will deposit
665 less charge and induce a smaller signal on the pick-up strips that could eventu-
666 ally not be detected. These two thresholds also restrain the overall geometrical
667 acceptance of the system.

668 **5.2.3.2 Simulation procedure**

669 The simulation software has been designed using C++ and the output data is saved
670 into ROOT histograms. Simulations start for a threshold T_{scint} varying in a range
671 from 0 to 45 mm in steps of 5 mm, where $T_{scint} = 0 \text{ mm}$ corresponds to the case
672 where there isn't any threshold apply on the input signal while $T_{scint} = 45 \text{ mm}$,
673 which is the scintillator thickness, is the case where muons cannot arrive orthogo-
674 nally onto the scintillator surface. For a given T_{scint} , a set of RPC thresholds are
675 considered. The RPC threshold, T_{RPC} varies from 2 mm, the thickness of the gas
676 volume, to 3 mm in steps of 0.25 mm. For each $(T_{scint}; T_{RPC})$ pair, $N_\mu = 10^8$
677 muons are randomly generated inside the muon plane described in the previous
678 paragraph with an azimuthal angle θ chosen to follow a $\cos^2\theta$ distribution.

679 Planes are associated to each surface of the scintillators. Knowing muon posi-
680 tion into the muon plane and its direction allows us, by assuming that muons travel
681 in a straight line, to compute the intersection of the muon track with these planes.
682 Applying conditions to the limits of the surfaces of the scintillator faces then gives
683 us an answer to whether or not the muon passed through the scintillators. In the
684 case the muon has indeed passed through the telescope, the path through each scin-
685 tillator is computed and muons whose path was shorter than T_{scint} are rejected and
686 are thus considered as having not interacted with the setup.

687 On the contrary, if the muon is labeled as good, its position within the RPC
688 plane is computed and the corresponding strip, determined by geometrical tests
689 in the case the distance through the gas volume was enough not to be rejected
690 because of T_{RPC} , gets a hit and several histograms are filled in order to keep
691 track of the generation point on the muon plane, the intersection points of the
692 reconstructed muons within the telescope, or on the RPC plane, the path traveled
693 through each individual scintillator or the gas volume, as well as other histograms.
694 Moreover, muons fill different histograms whether they are forward or backward
695 coming muons. They are discriminated according to their direction components.

696 When a muon is generated, an (x, y, z) position is assigned into the muon plane as
 697 well as a $(\theta; \phi)$ pair that gives us the direction it's coming from. This way, muons
 698 satisfying the condition $0 \leq \phi < \pi$ are designated as backward coming muons
 699 while muons satisfying $\pi \leq \phi < 2\pi$ as forward coming muons.

700 This simulation is then repeated for different telescope inclinations ranging in
 701 between 4 and 20° and varying in steps of 2° . Due to this inclination and to the
 702 vertical position of the detector under test, the muon distribution reconstructed in
 703 the detector plane is asymmetrical. The choice has been made to chose a skew
 704 distribution formula to fit the data built as the multiplication of gaussian and sig-
 705 moidal curves together. A typical gaussian formula is given as 5.1 and has three
 706 free parameters as A_g , its amplitude, \bar{x} , its mean value and σ , its root mean square.
 707 Sigmoidal curves as given by formula 5.2 are functions converging to 0 and A_s as
 708 x diverges. The inflexion point is given as x_i and λ is proportional to the slope at
 709 $x = x_i$. In the limit where $\lambda \rightarrow \infty$, the sigmoid becomes a step function.

$$g(x) = A_g e^{\frac{-(x-\bar{x})^2}{2\sigma^2}} \quad (5.1)$$

$$s(x) = \frac{A_s}{1 + e^{-\lambda(x-x_i)}} \quad (5.2)$$

710 Finally, a possible representation of a skew distribution is given by formula 5.3
 711 and is the product of 5.1 and 5.2. Naturally, here $A_{sk} = A_g \times A_s$ and represents
 712 the theoretical maximum in the limit where the skew tends to a gaussian function.

$$sk(x) = g(x) \times s(x) = A_{sk} \frac{e^{\frac{-(x-\bar{x})^2}{2\sigma^2}}}{1 + e^{-\lambda(x-x_i)}} \quad (5.3)$$

713 5.2.3.3 Results

714 Influence of T_{scint} on the muon distribution

715 Influence of T_{RPC} on the muon distribution

716 Influence of the telescope inclination on the muon distribution

717 Comparison to data taken at GIF without irradiation

718 5.2.4 Photon flux at GIF

719 5.2.4.1 Expectations from simulations

720 In order to understand and evaluate the γ flux in the GIF area, simulations had been
 721 conducted in 1999 and published by S. Agosteo et al [6]. Table 5.1 presented in
 722 this article gives us the γ flux for different distances D to the source. This sim-
 723 ulation was done using GEANT and a Monte Carlo N-Particle (MCNP) transport
 724 code, and the flux F is given in number of γ per unit area and unit time along with
 725 the estimated error from these packages expressed in %.

Nominal ABS	Photon flux F [$s^{-1}cm^{-2}$]			
	at $D = 50$ cm	at $D = 155$ cm	at $D = 300$ cm	at $D = 400$ cm
1	$0.12 \cdot 10^8 \pm 0.2\%$	$0.14 \cdot 10^7 \pm 0.5\%$	$0.45 \cdot 10^6 \pm 0.5\%$	$0.28 \cdot 10^6 \pm 0.5\%$
2	$0.68 \cdot 10^7 \pm 0.3\%$	$0.80 \cdot 10^6 \pm 0.8\%$	$0.25 \cdot 10^6 \pm 0.8\%$	$0.16 \cdot 10^6 \pm 0.6\%$
5	$0.31 \cdot 10^7 \pm 0.4\%$	$0.36 \cdot 10^6 \pm 1.2\%$	$0.11 \cdot 10^6 \pm 1.2\%$	$0.70 \cdot 10^5 \pm 0.9\%$

Table 5.1: Total photon flux ($E\gamma \leq 662$ keV) with statistical error predicted considering a ^{137}Cs activity of 740 GBq at different values of the distance D to the source along the x-axis of irradiation field [6].

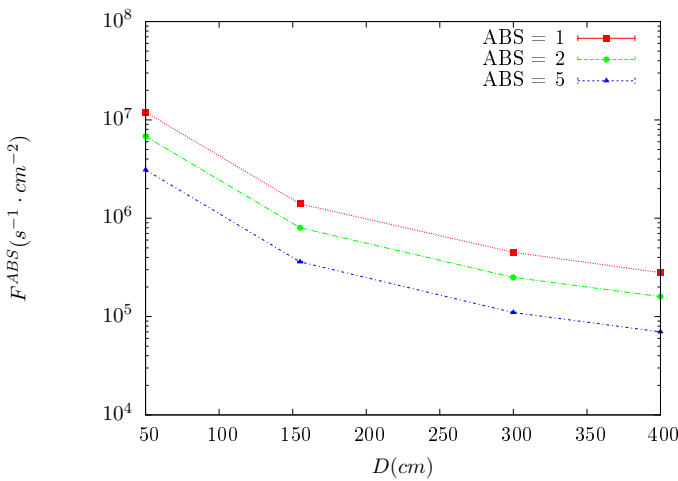


Figure 5.12: γ flux $F(D)$ is plot using values from table 5.1. As expected, the plot shows similar attenuation behaviours with increasing distance for each absorption factors.

726 The simulation doesn't directly provides us with an estimated flux at the level
 727 of our RPC. First of all, it is needed to extract the value of the flux from the
 728 available data contained in the original paper and then to estimate the flux in 2014
 729 at the time the experimentation took place. Figure 5.12 that contains the data from

730 Table 5.1. In the case of a pointlike source emitting isotropic and homogeneous
 731 gamma radiations, the gamma flux F at a distance D to the source with respect
 732 to a reference point situated at D_0 where a known flux F_0 is measured will be
 733 expressed like in Equation 5.4, assuming that the flux decreases as $1/D^2$, where c
 734 is a fitting factor.

$$F^{ABS} = F_0^{ABS} \times \left(\frac{cD_0}{D} \right)^2 \quad (5.4)$$

735 By rewriting Equation 5.4, it comes that :

$$c = \frac{D}{D_0} \sqrt{\frac{F^{ABS}}{F_0^{ABS}}} \quad (5.5)$$

$$\Delta c = \frac{c}{2} \left(\frac{\Delta F^{ABS}}{F^{ABS}} + \frac{\Delta F_0^{ABS}}{F_0^{ABS}} \right) \quad (5.6)$$

736 Finally, using Equation 5.5 and the data in Table 5.1 with $D_0 = 50$ cm as
 737 reference point, we can build Table 5.2. It is interesting to note that c for each
 738 value of D doesn't depend on the absorption factor.

Nominal ABS	Correction factor c		
	at $D = 155$ cm	at $D = 300$ cm	at $D = 400$ cm
1	$1.059 \pm 0.70\%$	$1.162 \pm 0.70\%$	$1.222 \pm 0.70\%$
2	$1.063 \pm 1.10\%$	$1.150 \pm 1.10\%$	$1.227 \pm 0.90\%$
5	$1.056 \pm 1.60\%$	$1.130 \pm 1.60\%$	$1.202 \pm 1.30\%$

Table 5.2: Correction factor c is computed thanks to formulae 5.5 taking as reference $D_0 = 50$ cm and the associated flux F_0^{ABS} for each absorption factor available in table 5.1.

739 For the range of D/D_0 values available, it is possible to use a simple linear
 740 fit to get the evolution of c . The linear fit will then use only 2 free parameters, a
 741 and b , as written in Equation 5.7. This gives us the results showed in Figure 5.13.
 742 Figure 5.13b confirms that using only a linear fit to extract c is enough as the
 743 evolution of the rate that can be obtained superimposes well on the simulation
 744 points.

$$c \left(\frac{D}{D_0} \right) = a \frac{D}{D_0} + b \quad (5.7)$$

$$F^{ABS} = F_0^{ABS} \left(a + \frac{bD_0}{D} \right)^2 \quad (5.8)$$

$$\Delta F^{ABS} = F^{ABS} \left[\frac{\Delta F_0^{ABS}}{F_0^{ABS}} + 2 \frac{\Delta a + \Delta b \frac{D_0}{D}}{a + \frac{bD_0}{D}} \right] \quad (5.9)$$

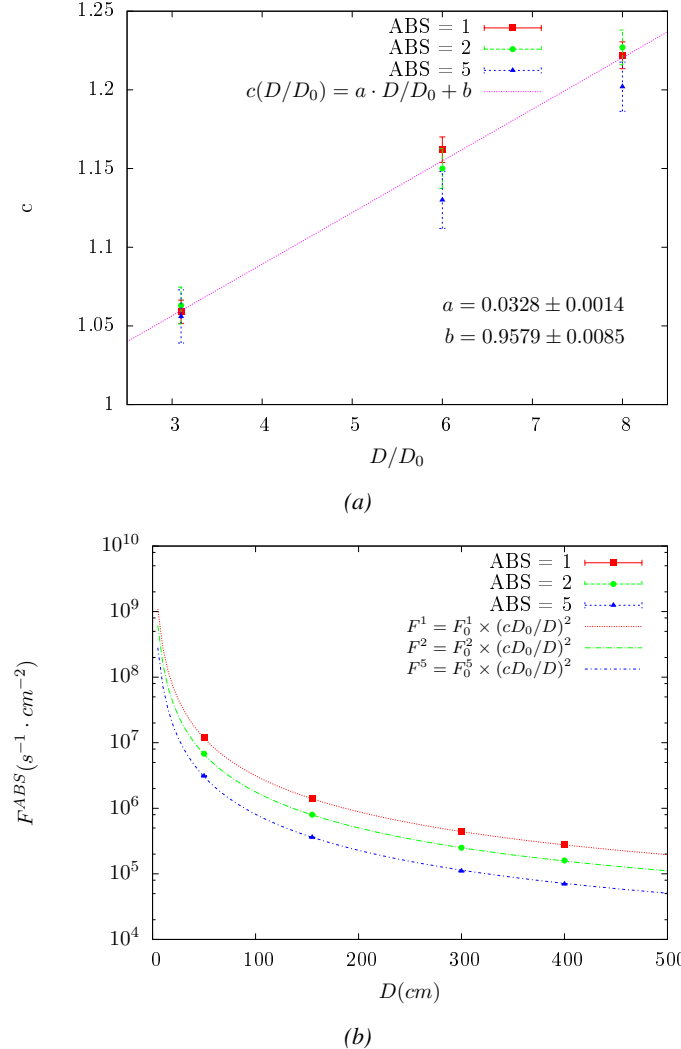


Figure 5.13: Figure 5.13a shows the linear approximation fit done via formulae 5.7 on data from table 5.2. Figure 5.13b shows a comparison of this model with the simulated flux using a and b given in figure 5.13a in formulae 5.4 and the reference value $D_0 = 50\text{cm}$ and the associated flux for each absorption factor F_0^{ABS} from table 5.1

In the case of the 2014 GIF tests, the RPC plane is located at a distance $D = 206\text{ cm}$ to the source. Moreover, to estimate the strength of the flux in 2014, it is necessary to consider the nuclear decay through time associated to the Cesium source whose half-life is well known ($t_{1/2} = (30.05 \pm 0.08)\text{ y}$). The very first source activity measurement has been done on the 5th of March 1997 while the

750 GIF tests were done between the 20th and the 31st of August 2014, i.e. at a
 751 time $t = (17.47 \pm 0.02)$ y resulting in an attenuation of the activity from 740 GBq
 752 in 1997 to 494 GBq in 2014. All the needed information to extrapolate the flux
 753 through our detector in 2014 has now been assembled, leading to the Table 5.3. It
 754 is interesting to note that for a common RPC sensitivity to γ of $2 \cdot 10^{-3}$, the order
 755 of magnitude of the estimated hit rate per unit area is of the order of the kHz for
 756 the fully opened source. Moreover, taking profit of the two working absorbers, it
 757 will be possible to scan background rates at 0 Hz, ~ 300 Hz as well as ~ 600 Hz.
 758 Without source, a good estimate of the intrinsic performance will be available.
 759 Then at 300 Hz, the goal will be to show that the detectors fulfill the performance
 760 certification of CMS RPCs. Then a first idea of the performance of the detectors at
 761 higher background will be provided with absorption factors 2 (~ 600 Hz) and 1 (no
 762 absorption). *[Here I will also put a reference to the plot showing the estimated
 763 background rate at the level of RE3/I in the case of HL-LHC but this one being
 764 in another chapter, I will do it later.]*

Nominal ABS	Photon flux F [$s^{-1}cm^{-2}$]			Hit rate/unit area [$Hz cm^{-2}$] at $D^{2014} = 206$ cm
	at $D_0^{1997} = 50$ cm	at $D_0^{1997} = 206$ cm	at $D^{2014} = 206$ cm	
1	$0.12 \cdot 10^8 \pm 0.2\%$	$0.84 \cdot 10^6 \pm 0.3\%$	$0.56 \cdot 10^6 \pm 0.3\%$	1129 ± 32
2	$0.68 \cdot 10^7 \pm 0.3\%$	$0.48 \cdot 10^6 \pm 0.3\%$	$0.32 \cdot 10^6 \pm 0.3\%$	640 ± 19
5	$0.31 \cdot 10^7 \pm 0.4\%$	$0.22 \cdot 10^6 \pm 0.3\%$	$0.15 \cdot 10^6 \pm 0.3\%$	292 ± 9

Table 5.3: The data at D_0 in 1997 is taken from [6]. In a second step, using Equations 5.8 and 5.9, the flux at D can be estimated in 1997. Then, taking into account the attenuation of the source activity, the flux at D can be estimated at the time of the tests in GIF in 2014. Finally, assuming a sensitivity of the RPC to γ $s = 2 \cdot 10^{-3}$, an estimation of the hit rate per unit area is obtained.

765 **5.2.4.2 Dose measurements**

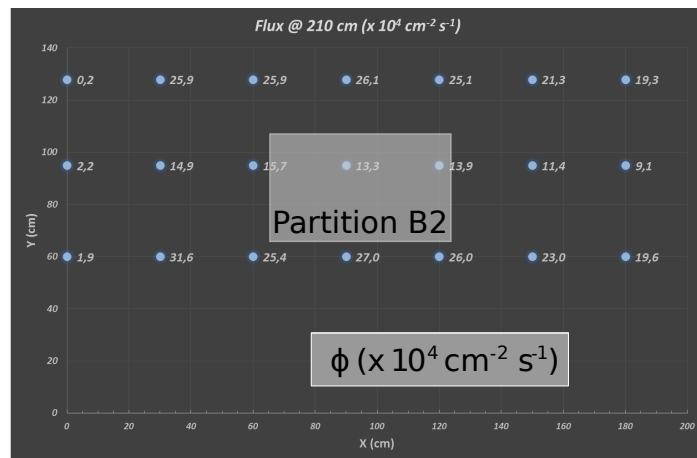


Figure 5.14: Dose measurements has been done in a plane corresponding to the tents front side. This plan is 1900 mm away from the source. As explained in the first chapter, a lens-shaped lead filter provides a uniform photon flux in the vertical plan orthogonal to the beam direction. If the second line of measured fluxes is not taken into account because of lower values due to experimental equipments in the way between the source and the tent, the uniformity of the flux is well showed by the results.

766 5.2.5 Results and discussions

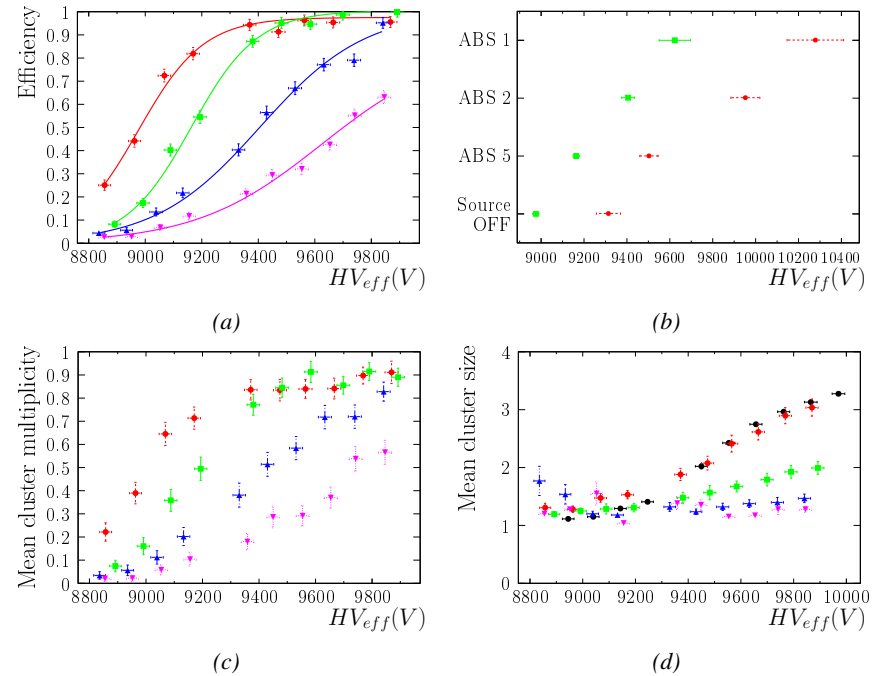


Figure 5.15

5.3 Longevity tests at GIF++

768 Longevity studies imply a monitoring of the performance of the detectors probed
769 using a high intensity muon beam in a irradiated environment by periodically mea-
770 suring their rate capability, the dark current running through them and the bulk
771 resistivity of the Bakelite composing their electrodes. GIF++, with its very intense
772 ^{137}Cs source, provides the perfect environment to perform such kind of tests. As-
773 suming a maximum acceleration factor of 3, it is expected to accumulate the equiv-
774 alent charge in 1.7 years.

775 As the maximum background is found in the endcap, the choice naturally was
776 made to focus the GIF++ longevity studies on endcap chambers. Most of the RPC
777 system was installed in 2007. Nevertheless, the large chambers in the fourth end-
778 cap (RE4/2 and RE4/3) have been installed during LS1 in 2014. The Bakelite of
779 these two different productions having different properties, four spare chambers
780 of the present system were selected, two RE2,3/2 spares and two RE4/2 spares.
781 Having two chambers of each type allows to always keep one of them non irradia-
782 ted as reference, the performance evolution of the irradiated chamber being then
783 compared through time to the performance of the non irradiated one.

784 The performance of the detectors under different level of irradiation is measured
785 periodically during dedicated test beam periods using the H4 muon beam. In be-
786 tween these test beam periods, the two RE2,3/2 and RE4/2 chambers selected for
787 this study are irradiated by the ^{137}Cs source in order to accumulate charge and
788 the gamma background is monitored, as well as the currents. The two remaining
789 chambers are kept non-irradiated as reference detectors. Due to the limited gas
790 flow in GIF++, the RE4 chamber remained non-irradiated until end of November
791 2016 where a new mass flow controller has been installed allowing for bigger vol-
792 umes of gas to flow in the system.

793 Figures 5.16 and 5.17 give us for different test beam periods, and thus for in-
794 creasing integrated charge through time, a comparison of the maximum efficiency,
795 obtained using a sigmoid-like function, and of the working point of both irradiated
796 and non irradiated chambers [8]. No aging is yet to see from this data, the shifts in
797 γ rate per unit area in between irradiated and non irradiated detectors and RE2 and
798 RE4 types being easily explained by a difference of sensitivity due to the various
799 Bakelite resistivities of the HPL electrodes used for the electrode production.

800 Collecting performance data at each test beam period allows us to extrapolate the
801 maximum efficiency for a background hit rate of 300 Hz/cm^2 corresponding to
802 the expected HL-LHC conditions. Aging effects could emerge from a loss of ef-
803 ficiency with increasing integrated charge over time, thus Figure 5.18 helps us
804 understand such degradation of the performance of irradiated detectors in compar-
805 ison with non irradiated ones. The final answer for an eventual loss of efficiency is
806 given in Figure 5.19 by comparing for both irradiated and non irradiated detectors

807 the efficiency sigmoids before and after the longevity study. Moreover, to complete
 808 the performance information, the Bakelite resistivity is regularly measured thanks
 809 to Ag scans (Figure 5.20) and the noise rate is monitored weekly during irradiation
 810 periods (Figure 5.21). At the end of 2016, no signs of aging were observed and
 811 further investigation is needed to get closer to the final integrated charge require-
 812 ments proposed for the longevity study of the present CMS RPC sub-system.

813

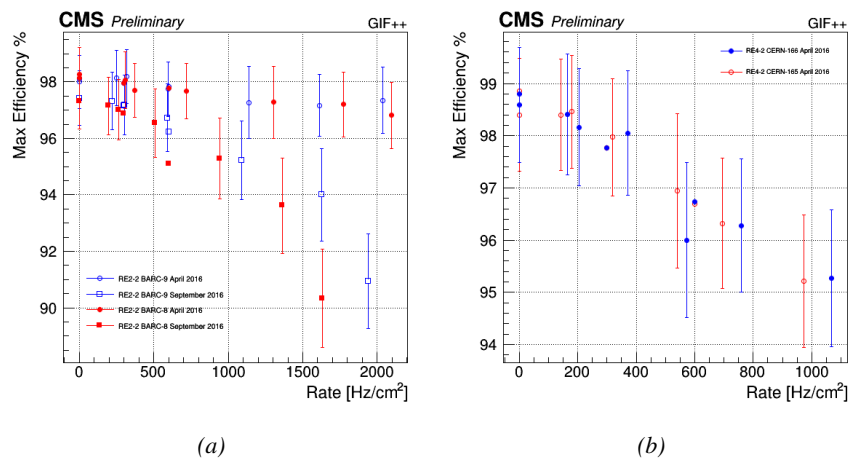


Figure 5.16: Evolution of the maximum efficiency for RE2 (5.16a) and RE4 (5.16b) chambers with increasing extrapolated γ rate per unit area at working point. Both irradiated (blue) and non irradiated (red) chambers are shown.

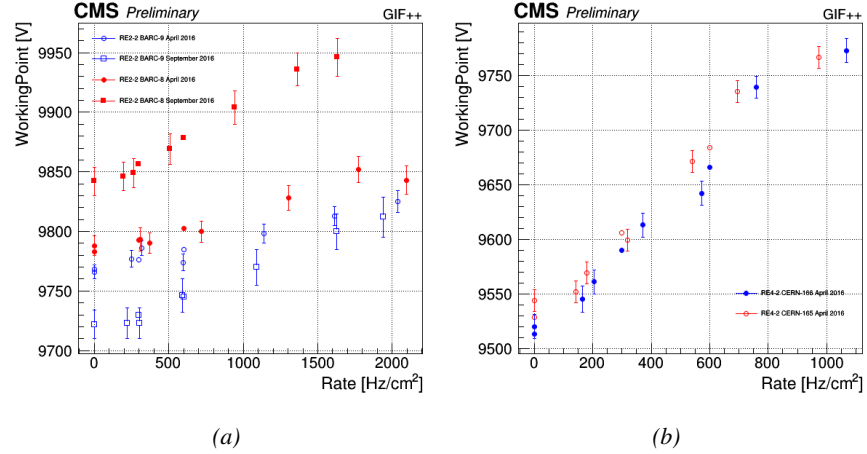


Figure 5.17: Evolution of the working point for RE2 (5.17a) and RE4 (5.17b) with increasing extrapolated γ rate per unit area at working point. Both irradiated (blue) and non irradiated (red) chambers are shown.

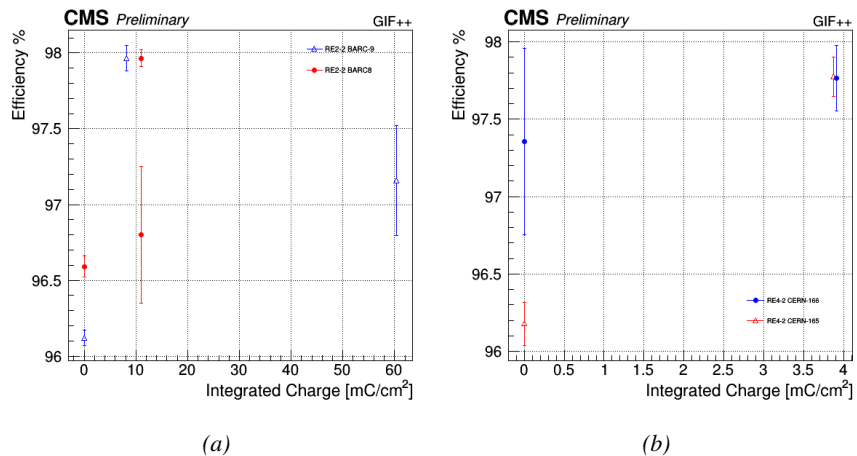


Figure 5.18: Evolution of the maximum efficiency at HL-LHC conditions, i.e. a background hit rate per unit area of 300 Hz/cm², with increasing integrated charge for RE2 (5.18a) and RE4 (5.18b) detectors. Both irradiated (blue) and non irradiated (red) chambers are shown. The integrated charge for non irradiated detectors is recorded during test beam periods and stays small with respect to the charge accumulated in irradiated chambers.

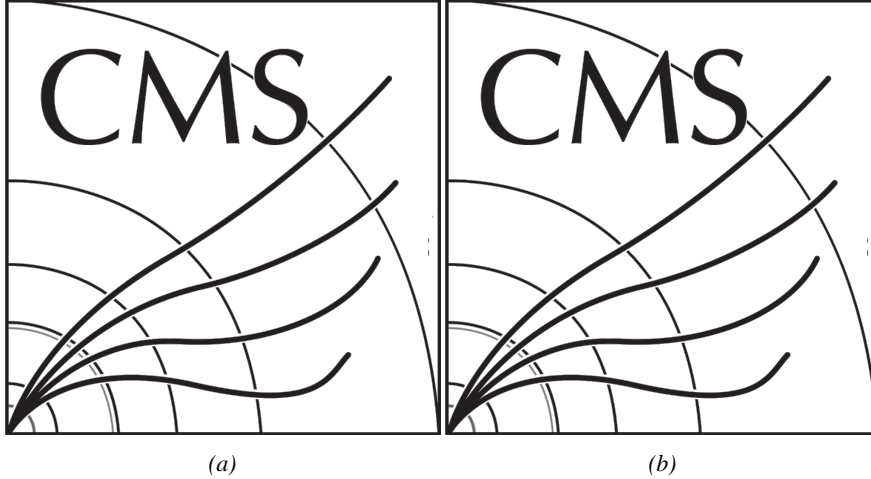


Figure 5.19: Comparison of the efficiency sigmoid before (triangles) and after (circles) irradiation for RE2 (5.19a) and RE4 (5.19b) detectors. Both irradiated (blue) and non irradiated (red) chambers are shown.

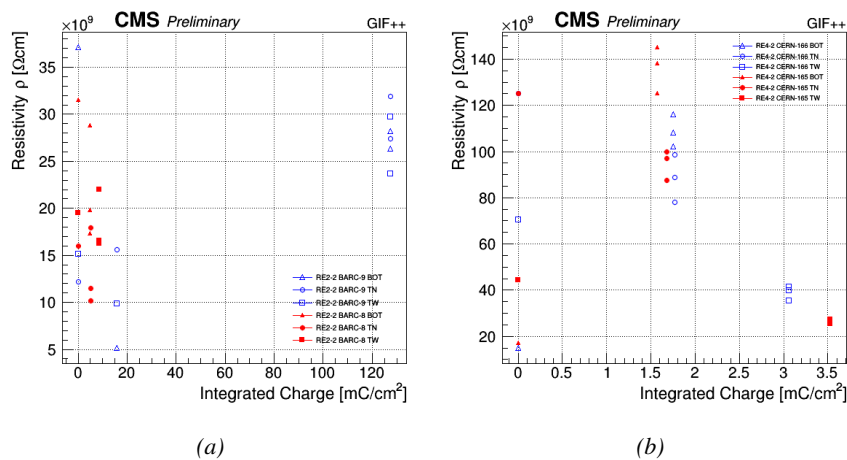


Figure 5.20: Evolution of the Bakelite resistivity for RE2 (5.20a) and RE4 (5.20b) detectors. Both irradiated (blue) and non irradiated (red) chambers are shown.

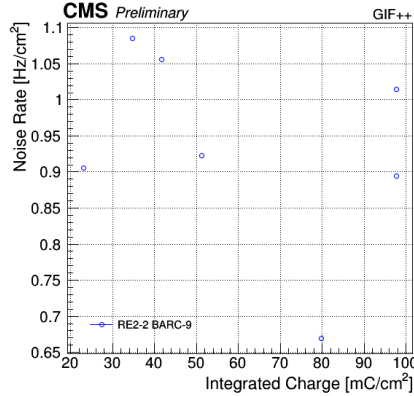


Figure 5.21: Evolution of the noise rate per unit area for the irradiated chamber RE2-2-BARC-9 only.

5.3.1 Description of the Data Acquisition

For the longevity studies, four spare chambers of the present system are used. Two spare RPCs of the RE2,3 stations as well as two spare RPCs from the new RE4 stations have been mounted in a Trolley. Six RE4 gaps are also placed in the trolley. The trolley is placed inside the GIF++ in the upstream region of the bunker, taking the cesium source as a reference. The trolley is oriented for the detection surface of the chambers to be orthogonal to the beam line. The system can be moved along the orthogonal plane in order to have the beam in all η -partitions. For the aging the trolley is moved outside the beam line and is placed in a distance of 5.2 m to the source, which irradiates the bunker using an attenuation filter of 2.2 which corresponds to a fluence of 10^7 gamma/cm².

During GIF++ operation, the data collected can be divided into different categories as several parameters are monitored in addition to the usual RPC performance data. On one hand, to know the performance of a chamber, it is need to measure its efficiency and to know the background conditions in which it is operated. To do this, the hit signals from the chamber are recorded and stored in a ROOT file via a Data Acquisition (DAQ) software. On the other hand, it is also very important to monitor parameters such as environmental pressure and temperature, gas temperature and humidity, RPC HV, LV, and currents, or even source and beam status. This is done through the GIF++ web Detector Control Software (DCS) that stores this information in a database.

Two different types of tests are conducted on RPCs via the DAQ. Indeed, the performance of the detectors is measured periodically during dedicated test beam periods using the H4 muon beam. In between these test beam periods, when the beam is not available, the chambers are irradiated by the ^{137}Cs in order to accu-

839 mulate deposited charge and the gamma background is measured.

840 RPCs under test are connected through LVDS cables to V1190A Time-to-
 841 Digital Converter (TDC) modules manufactured by CAEN. These modules, lo-
 842 cated in the rack area outside of the bunker, get the logic signals sent by the cham-
 843 bers and save them into their buffers. Due to the limited size of the buffers, the
 844 collected data is regularly erased and replaced. A trigger signal is needed for the
 845 TDC modules to send the useful data to the DAQ computer via a V1718 CAEN
 846 USB communication module.

847 In the case of performance test, the trigger signal used for data acquisition is
 848 generated by the coincidence of three scintillators. A first one is placed upstream
 849 outside of the bunker, a second one is placed downstream outside of the bunker,
 850 while a third one is placed in front of the trolley, close by the chambers. Every time
 851 a trigger is sent to the TDCs, i.e. every time a muon is detected, knowing the time
 852 delay in between the trigger and the RPC signals, signals located in the right time
 853 window are extracted from the buffers and saved for later analysis. Signals are
 854 taken in a time window of 400 ns centered on the muon peak (here we could show
 855 a time spectrum). On the other hand, in the case of background rate measurement,
 856 the trigger signal needs to be "random" not to measure muons but to look at gamma
 857 background. A trigger pulse is continuously generated at a rate of 300 Hz using a
 858 dual timer. To integrate an as great as possible time, all signals contained within
 859 a time window of 10us prior to the random trigger signal are extracted form the
 860 buffers and saved for further analysis (here another time spectrum to illustrate
 861 could be useful, maybe even place both spectrum together as a single Figure).

862 The signals sent to the TDCs correspond to hit collections in the RPCs. When a
 863 particle hits a RPC, it induce a signal in the pickup strips of the RPC readout. If this
 864 signal is higher than the detection threshold, a LVDS signal is sent to the TDCs.
 865 The data is then organised into 4 branches keeping track of the event number, the
 866 hit multiplicity for the whole setup, and the time and channel profile of the hits in
 867 the TDCs.

868 **5.3.2 RPC current, environmental and operation parameter mon- 869 itoring**

870 In order to take into account the variation of pressure and temperature between
 871 different data taking periods the applied voltage is corrected following the rela-
 872 tionship :

$$873 \quad HV_{eff} = HV_{app} \times \left(0.2 + 0.8 \cdot \frac{P_0}{P} \times \frac{T}{T_0} \right) \quad (5.10)$$

873 where T_0 (=293 K) and P_0 (=990 mbar) are the reference values.

874 5.3.3 Measurement procedure

- 875 Insert a short description of the online tools (DAQ, DCS, DQM).
- 876 Insert a short description of the offline tools : tracking and efficiency algorithm.
- 877 Identify long term aging effects we are monitoring the rates per strip.

878 5.3.4 Longevity studies results

6

879

880

Investigation on high rate RPCs

881 **6.1 Rate limitations and ageing of RPCs**

882 **6.1.1 Low resistivity electrodes**

883 **6.1.2 Low noise front-end electronics**

884 **6.2 Construction of prototypes**

885 **6.3 Results and discussions**

7

886

887

Conclusions and outlooks

888 **7.1 Conclusions**

889 **7.2 Outlooks**

References

890

- 891 [1] CERN. Geneva. LHC Experiments Committee. *The CMS muon project :
892 Technical Design Report*. Tech. rep. CERN-LHCC-97-032. CMS Collabora-
893 ration, 1997.
- 894 [2] CERN. Geneva. LHC Experiments Committee. *Technical Proposal for the
895 Phase-II Upgrade of the CMS Detector*. Tech. rep. CERN-LHCC-2015-010.
896 CMS Collaboration, 2015.
- 897 [3] CERN. Geneva. LHC Experiments Committee. *CMS, the Compact Muon
898 Solenoid : technical proposal*. Tech. rep. CERN-LHCC-94-38. CMS Col-
899 laboration, 1994.
- 900 [4] M. Abbrescia et al. “Study of long-term performance of CMS RPC under
901 irradiation at the CERN GIF”. In: *NIMA* 533 (2004), pp. 102–106.
- 902 [5] H.C. Kim et al. “Quantitative aging study with intense irradiation tests for
903 the CMS forward RPCs”. In: *NIMA* 602 (2009), pp. 771–774.
- 904 [6] S. Agosteo et al. “A facility for the test of large-area muon chambers at high
905 rates”. In: *NIMA* 452 (2000), pp. 94–104.
- 906 [7] PoS, ed. *CERN GIF ++ : A new irradiation facility to test large-area par-
907 ticle detectors for the high-luminosity LHC program*. Vol. TIPP2014. 2014,
908 pp. 102–109.
- 909 [8] M. Abbrescia et al. “Cosmic ray tests of double-gap resistive plate chambers
910 for the CMS experiment”. In: *NIMA* 550 (2005), pp. 116–126.
- 911 [9] A. Fagot. *GIF++ DAQ v4.0*. 2017. URL: https://github.com/afagot/GIF_DAQ.
- 913 [10] CAEN. *Mod. V1190-VX1190 A/B, 128/64 Ch Multihit TDC*. 14th ed. 2016.
- 914 [11] CAEN. *Mod. V1718 VME USB Bridge*. 9th ed. 2009.
- 915 [12] W-Ie-Ne-R. *VME 6021-23 VXI*. 5th ed. 2016.

A

916

917 A data acquisition software for CAEN 918 VME TDCs

919 Certifying detectors in the perspective of HL-LHC required to develop tools for the
920 GIF++ experiment. Among them was the C++ Data Acquisition (DAQ) software
921 that allows to make the communications in between the computer and the TDC
922 modules in order to retrieve the RPC data [9]. In this appendix, details about the
923 software, as of how the software was written, how it functions and how it can be
924 exported to another similar setup.

925 **A.1 GIF++ DAQ file tree**

926 GIF++ DAQ source code is fully available on github at https://github.com/afagot/GIF_DAQ. The software requires 3 non-optional dependencies:

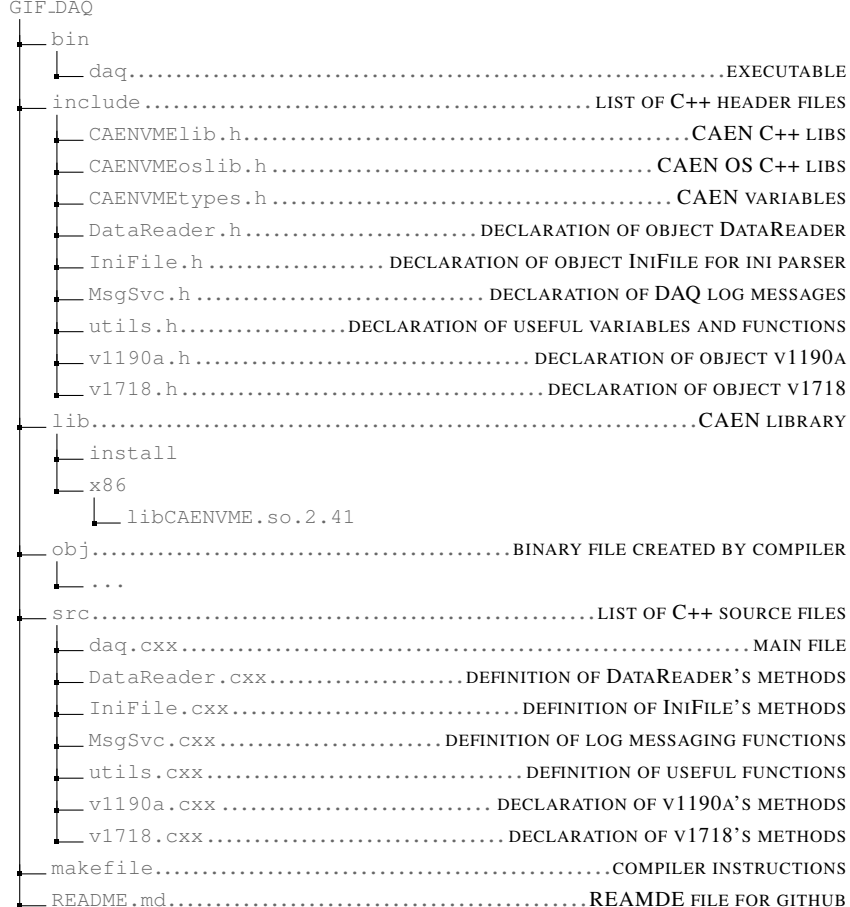
- 928 • CAEN USB Driver to mount the VME hardware
- 929 • CAEN VME Library to communicate with the VME hardware
- 930 • ROOT to organize the collected data into a TTree

931 The CAEN VME library will not be packaged by distributions and will need
932 to be installed manually. To compile the GIF++ DAQ project via a terminal, from
933 the DAQ folder use the command :

934 `make`

935 The source code tree is provided below along with comments to give an overview
 936 of the files' content. The different objects created for this project (v1718, v1190a,
 937 IniFile & DataReader) will be described in details in the following sections.

938



939 A.2 Description of the readout setup

940 The CMS RPC setup at GIF++ counts 5 V1190A Time-to-Digital Converter (TDC)
 941 manufactured by CAEN [10]. V1190A are VME units accepting 128 independent
 942 Multi-Hit/Multi-Event TDC channels whose signals are treated by 4 100 ps high
 943 performance TDC chips developped by CERN / ECP-MIC Division. The com-
 944 munication between the computer and the TDCs to transfer data is done via a
 945 V1718 VME master module also manufactured by CAEN and operated from a
 946 USB port [11]. These VME modules are all hosted into a 6U VME 6021 pow-

⁹⁴⁷ ered crate manufactured by W-Ie-Ne-R than can accomodate up to 21 VME bus
⁹⁴⁸ cards [12]. These 3 components of the DAQ setup are shown in Figure A.1.

⁹⁴⁹

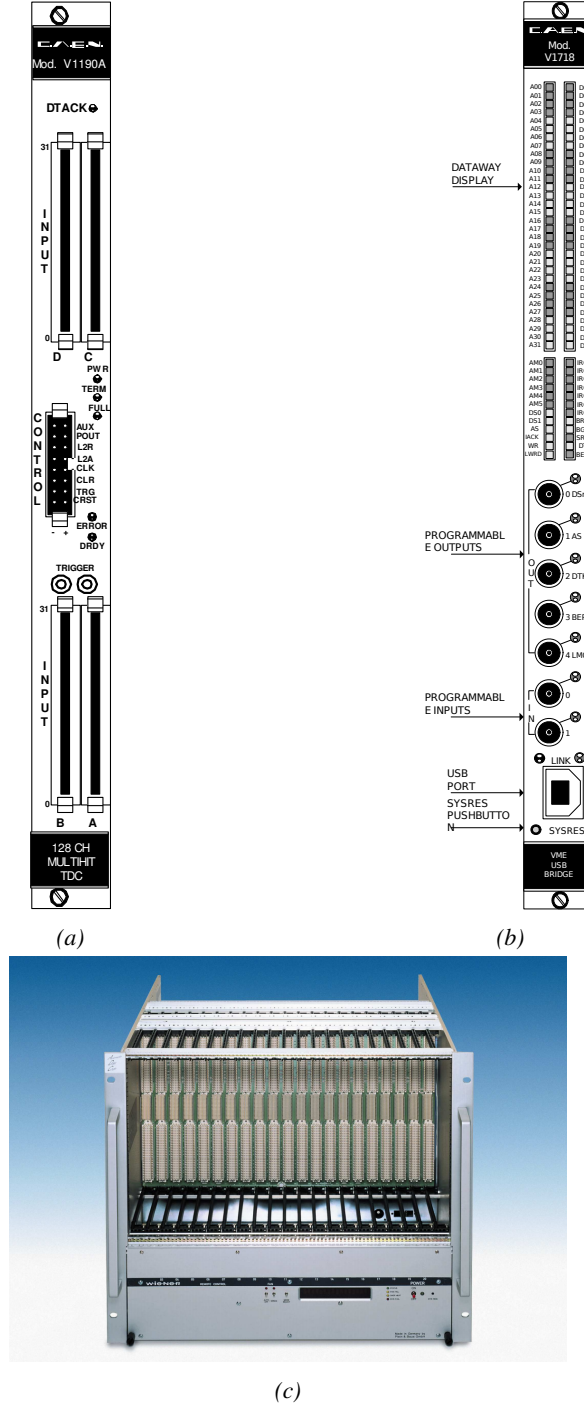


Figure A.1: (A.1a) View of the front panel of a V1190A TDC module [10]. (A.1b) View of the front panel of a V1718 Bridge module [11]. (A.1c) View of the front panel of a 6U 6021 VME crate [12].

950 A.3 Data read-out

951 To efficiently perform a data readout algorithm, C++ objects to handle the VME
 952 modules (TDCs and VME bridge) have been created along with objects to store
 953 data and read the configuration file that comes as an input of the DAQ software.
 954 It is useful to remind that the DAQ software in GIF++ is not a standalone software
 955 but is called through a Web Detector Control System (webDCS) application, that
 956 is the core of interactions with GIF++ setup, when data needs to be taken. Nev-
 957 ertheless, it is straight forward to make it into a standalone program that could be
 958 adapted to any VME setup using V1190A and V1718 modules.

959

960 A.3.1 V1190A TDCs

961 The DAQ used at GIF takes profit of the *Trigger Matching Mode* offered by V1190A
 962 modules. This setting is enabled through the method `v1190a::SetTrigMatching`
 963 (`int ntdcs`) where `ntdcs` is the total number of TDCs in the setup this setting
 964 needs to be enabled for (Source Code A.1). A trigger matching is performed in
 965 between a trigger time tag, a trigger signal sent into the TRIGGER input of the
 966 TDC visible on Figure A.1a, and the channel time measurements, signals recorded
 967 from the detectors under test in our case. Control over this data acquisition mode,
 968 explained through Figure A.2, is offered via 4 programmable parameters:

969 • **match window:** the matching between a trigger and a hit is done within a
 970 programmable time window. This is set via the method
 971 `void v1190a::SetTrigWindowWidth(Uint windowHeight, int ntdcs)`

972 • **window offset:** temporal distance between the trigger tag and the start of
 973 the trigger matching window. This is set via the method
 974 `void v1190a::SetTrigWindowWidth(Uint windowHeight, int ntdcs)`

975 • **extra search margin:** an extended time window is used to ensure that all
 976 matching hits are found. This is set via the method
 977 `void v1190a::SetTrigSearchMargin(Uint searchMargin, int ntdcs)`

978 • **reject margin:** older hits are automatically rejected to prevent buffer over-
 979 flows and to speed up the search time. This is set via the method
 980 `void v1190a::SetTrigRejectionMargin(Uint rejectMargin, int ntdcs)`

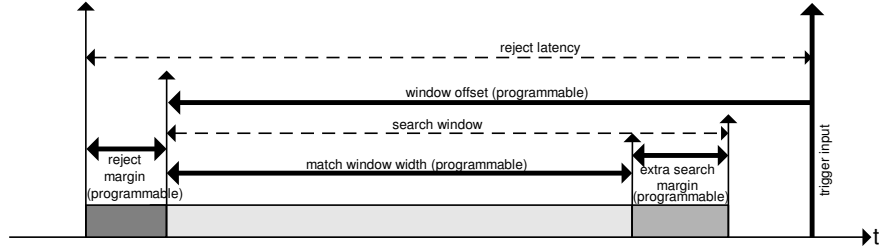


Figure A.2: Module V1190A Trigger Matching Mode timing diagram [10].

981 Each of these 4 parameters are given in number of clocks, 1 clock being 25 ns
 982 long. It is easy to understand at this level that there are 3 possible functioning
 983 settings:

- 984 • **1:** the match window is entirely contained after the trigger signal,
 985 • **2:** the match window overlaps the trigger signal, or
 986 • **3:** the match window is entirely contained before the trigger signal as dis-
 987 played on Figure A.2.

988 In both the first and second cases, the sum of the window width and of the
 989 offset can be set to a maximum of 40 clocks, which corresponds to 1 μ s. Evidently,
 990 the offset can be negative, allowing for a longer match window, with the constraint
 991 of having the window ending at most 1 μ s after the trigger signal. In the third case,
 992 the maximum negative offset allowed is of 2048 clocks (12 bit) corresponding to
 993 51.2 μ s, the match window being strictly smaller than the offset. In the case of
 994 GIF++, the choice has been made to use this last setting by delaying the trigger
 995 signal. During the studies performed in GIF++, both the efficiency of the RPCs,
 996 probed using a muon beam, and the noise or gamma background rate are moni-
 997 tored. The extra search and reject margins are left unused.

998 To probe the efficiency of RPC detectors, the trigger time tag is provided by the
 999 coincidence of scintillators when a bunch of muons passes through GIF++ area is
 1000 used to trigger the data acquisition. For this measurement, it is useful to reduce the
 1001 match window width only to contain the muon information. Indeed, the delay in
 1002 between a trigger signal and the detection of the corresponding muon in the RPC
 1003 being very constant (typically a few tens of ns due to jitter and cable length), the
 1004 muon signals are very localised in time. Thus, due to a delay of approximalety
 1005 325 ns in between the muons and the trigger, the settings where chosen to have a
 1006 window width of 24 clocks (600 ns) centered on the muon peak thanks to a nega-
 1007 tive offset of 29 clocks (725 ns).

1008 On the otherhand, monitoring the rates don't require for the DAQ to look at a
 1009 specific time window. It is important to integrate enough time to have a robust

1010 measurement of the rate as the number of hits per time unit. The triggerring signal
 1011 is provided by a pulse generator at a frequency of 300 Hz to ensure that the
 1012 data taking occurs in a random way, with respect to beam physics, to probe only
 1013 the irradiation spectrum on the detectors. The match window is set to 400 clocks
 1014 (10 µs) and the negative offset to 401 clocks as it needs to exceed the value of the
 1015 match window.

1016

Source Code A.1: Description of C++ object v1190a.

```

1017
1018 class v1190a
1019 {
1020     private :
1021         long             Handle;
1022         vector<Data32>   Address;
1023         CVDataWidth      DataWidth;
1024         CVAddressModifier AddressModifier;
1025
1026     public:
1027
1028         v1190a(long handle, IniFile *inifile, int ntdcs);
1029         ~v1190a();
1030         Data16 write_op_reg(Data32 address, int code, string error);
1031         Data16 read_op_reg(Data32 address, string error);
1032         void Reset(int ntdcs);
1033         void Clear(int ntdcs);
1034         void TestWR(Data16 value,int ntdcs);
1035         void CheckTDCStatus(int ntdcs);
1036         void CheckCommunication(int ntdcs);
1037         void SetTDCTestMode(Data16 mode,int ntdcs);
1038         void SetTrigMatching(int ntdcs);
1039         void SetTrigTimeSubtraction(Data16 mode,int ntdcs);
1040         void SetTrigWindowWidth(Uint windowHeight,int ntdcs);
1041         void SetTrigWindowOffset(Uint windowOffset,int ntdcs);
1042         void SetTrigSearchMargin(Uint searchMargin,int ntdcs);
1043         void SetTrigRejectionMargin(Uint rejectMargin,int ntdcs);
1044         void GetTrigConfiguration(int ntdcs);
1045         void SetTrigConfiguration(IniFile *inifile,int ntdcs);
1046         void SetTDCDetectionMode(Data16 mode,int ntdcs);
1047         void SetTDCResolution(Data16 lsb,int ntdcs);
1048         void SetTDCDeadTime(Data16 time,int ntdcs);
1049         void SetTDCHeadTrailer(Data16 mode,int ntdcs);
1050         void SetTDCEventSize(Data16 size,int ntdcs);
1051         void SwitchChannels(IniFile *inifile,int ntdcs);
1052         void SetIRQ(Data32 level, Data32 count,int ntdcs);
1053         void SetBlockTransferMode(Data16 mode,int ntdcs);
1054         void Set(IniFile *inifile,int ntdcs);
1055         void CheckStatus(CVErrorCodes status) const;
1056         int ReadBlockD32(Uint tdc, const Data16 address,
1057                         Data32 *data, const Uint words, bool ignore_berr);
1058         Uint  Read(RAWData *DataList,int ntdcs);
1059     };

```

1019 The v1190a object, defined in the DAQ software as in Source Code A.1, offers
 1020 the possibility to concatenate all TDCs in the readout setup into a single object con-

1021 taining a list of hardware addresses (addresses to access the TDCs' buffer through
 1022 the VME crate) and each constructor and method acts on the list of TDCs.

1023

1024 A.3.2 DataReader

1025 Enabled thanks to `v1190a::SetBlockTransferMode(Data16 mode, int ntdcs)`,
 1026 the data transfer is done via Block Transfer (BLT). Using BLT allows to tranfer a
 1027 fixed number of events called a *block*. This is used together with an Almost Full
 1028 Level (AFL) of the TDCs' output buffers, defined through `v1190a::SetIRQ(Data32`
 1029 `level, Data32 count, int ntdcs)`. This AFL gives the maximum amount of
 1030 32735 words (16 bits, corresponding to the depth of a TDC output buffer) that
 1031 can wrten in a buffer before an Interrupt Request (IRQ) is generated and seen by
 1032 the VME Bridge, stopping the data acquisition to transfer the content of each TDC
 1033 buffers before resuming. For each trigger, 6 words or more are written into the
 1034 TDC buffer:

1035 • a **global header** providing information of the event number since the begin-
 1036 ning of the data acquisition,

1037 • a **TDC header**,

1038 • the **TDC data** (*if any*), 1 for each hit recorded during the event, providing
 1039 the channel and the time stamp associated to the hit,

1040 • a **TDC error** providing error flags,

1041 • a **TDC trailer**,

1042 • a **global trigger time tag** that provides the absolute trigger time relatively
 1043 to the last reset, and

1044 • a **global trailer** providing the total word count in the event.

1045 As previously described in Section 4.4.3, CMS RPC FEEs provide us with
 1046 100 ns long LVDS output signals that are injected into the TDCs' input. Any
 1047 avalanche signal that gives a signal above the FEEs threshold is thus recorded by
 1048 the TDCs as a hit within the match window. Each hit is assigned to a specific TDC
 1049 channel with a time stamp, with a precision of 100 ps. The reference time, $t_0 = 0$,
 1050 is provided by the beginning of the match window. Thus for each trigger, coming
 1051 from a scintillator coïncidence or the pulse generator, a list of hits is stored into
 1052 the TDCs' buffers and will then be transferred into a ROOT Tree.

1053

1054 When the BLT is used, it is easy to understand that the maximum number of
 1055 words that have been set as AFL will not be a finite number of events or, at least,

1056 the number of events that would be recorded into the TDC buffers will not be a
 1057 multiple of the block size. In the last BLT cycle to tranfer data, the number of
 1058 events to transfer will most propably be lower than the block size. In that case, the
 1059 TDC can add fillers at the end of the block but this option requires to send more
 1060 data to the computer and is thus a little slower. Another solution is to finish the
 1061 transfer after the last event by sending a bus error that states that the BLT reached
 1062 the last event in the pile. This method has been chosen in GIF++.

1063
 1064 Due to irradiation, an event in GIF++ can count up to 300 words per TDC. A
 1065 limit of 4096 words (12 bits) has been set to generate IRQ which represent from
 1066 14 to almost 700 events depending on the average of hits collected per event. Then
 1067 the block size has been set to 100 events with enabled bus errors. When an AFL
 1068 is reached for one of the TDCs, the VME bridge stops the acquisition by sending
 1069 a BUSY signal.

1070
 1071 The data is then transferred one TDC at a time into a structure called `RAWData`
 1072 (Source Code A.2).

1073

1074 *Source Code A.2: Description of data holding C++ structure `RAWData`.*

```
1075 struct RAWData{
 1076   vector<int>           *EventList;
 1077   vector<int>           *NHitsList;
 1078   vector<int>           *QFlagList;
 1079   vector<vector<int>>    *ChannelList;
 1080   vector<vector<float>>  *TimeStampList;
 1081 };
```

1076 In order to organize the data transfer and the data storage, an object called
 1077 `DataReader` was created (Source Code A.3). On one hand, it has `v1718` and `v1190a`
 1078 objects as private members for communication purposes, such as VME modules
 1079 settings via the configuration file `*iniFile` or data read-out through `v1190a::Read()`
 1080 and on the other hand, it contains the struture `RAWData` that allows to organise the
 1081 data in vectors reproducing the tree structre of a ROOT file.

1082

1083 *Source Code A.3: Description of C++ object `DataReader`.*

```

class DataReader
{
    private:
        bool      StopFlag;
        IniFile *iniFile;
        Data32   MaxTriggers;
        v1718    *VME;
        int       nTDCs;
        v1190a   *TDCs;
        RAWData  TDCData;

    public:
        DataReader();
        virtual ~DataReader();
        void     SetIniFile(string inifilename);
        void     SetMaxTriggers();
        Data32  GetMaxTriggers();
        void     SetVME();
        void     SetTDC();
        int      GetQFlag(Uint it);
        void     Init(string inifilename);
        void     FlushBuffer();
        void     Update();
        string  GetFileName();
        void     WriteRunRegistry(string filename);
        void     Run();
};

1085      Each event is transferred from TDCData and saved into branches of a ROOT
1086      TTree as 3 integers that represent the event ID (EventCount), the number of hits
1087      read from the TDCs (nHits), and the quality flag that provides information for any
1088      problem in the data transfer (qflag), and 2 lists of nHits elements containing the
1089      fired TDC channels (TDCh) and their respective time stamps (TDCTS), as presented
1090      in Source Code A.4. An example of ROOT data file is provided with Figure A.3.
1091

```

*Source Code A.4: Highlight of the data transfer and organisation within
`DataReader::Run()` after the data has been collected into `TDCData`.*

```
RAWData TDCData;
TFile *outputFile = new TFile(outputFileName.c_str(), "recreate");
TTree *RAWDataTree = new TTree("RAWData", "RAWData");

int EventCount = -9;
int nHits = -8;
int qflag = -7;
vector<int> TDCCh;
vector<float> TDCTS;

RAWDataTree->Branch("EventNumber", &EventCount, "EventNumber/I");
RAWDataTree->Branch("number_of_hits", &nHits, "number_of_hits/I");
RAWDataTree->Branch("Quality_flag", &qflag, "Quality_flag/I");
RAWDataTree->Branch("TDC_channel", &TDCCh);
RAWDataTree->Branch("TDC_TimeStamp", &TDCTS);

1093
//...
//Here read the TDC data using v1190a::Read() and place it into
//TDCData for as long as you didn't collect the requested amount
//of data.
//...

for(Uint i=0; i<TDCData.EventList->size(); i++) {
    EventCount = TDCData.EventList->at(i);
    nHits = TDCData.NHitsList->at(i);
    qflag = TDCData.QFlagList->at(i);
    TDCCh = TDCData.ChannelList->at(i);
    TDCTS = TDCData.TimeStampList->at(i);
    RAWDataTree->Fill();
}
```

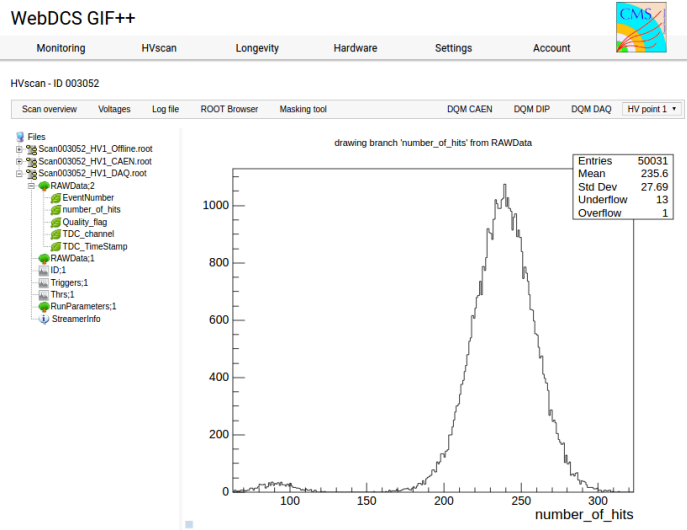


Figure A.3: Structure of the ROOT output file generated by the DAQ. The 5 branches (EventNumber, number_of_hits, Quality_flag, TDC_channel and TDC_TimeStamp) are visible on the left panel of the ROOT browser. On the right panel is visible the histogram corresponding to the variable nhits. In this specific example, there were approximately 50k events recorded to measure the gamma irradiation rate on the detectors. Each event is stored as a single entry in the TTree.

1094 A.3.3 V1718 USB Bridge

1095 In the previous section, the data transfer has been discussed. The importance of
 1096 the v1718 object (Source Code A.6), used as private member of DataReader,
 1097 was not explicated. VME master modules are used for communication purposes
 1098 as they host the USB port that connects the powered crate buffer to the com-
 1099 puter where the DAQ is installed. From the source code point of view, this ob-
 1100 ject is used to control the communication status, by reading the returned error
 1101 codes with v1718::CheckStatus(), or to check for IRQs coming from the TDCs
 1102 through v1718::CheckIRQ(). Finally, to ensure that triggers are blocked at the
 1103 hardware level, a NIM pulse is sent out of one of the 5 programmable outputs
 1104 (v1718::SendBUSY()) to the VETO of the coincidence module where the trigger
 1105 signals originate from. As long as this signal is ON, no trigger can reach the TDCs
 1106 anymore.

1107

1108 *Source Code A.5: Description of C++ object v1718.*

```

class v1718{
    private:
        int             Handle;
        Data32          Data;           // Data
        CVIRQLevels     Level;         // Interrupt level
        CVAddressModifier AM;          // Addressing Mode
        CVDataWidth     DataSize;      // Data Format
        Data32          BaseAddress;   // Base Address

    public:
        v1718(IniFile *inifile);
        ~v1718();
        long            GetHandle(void) const;
        int             SetData(Data16 data);
        Data16          GetData(void);
        int             SetLevel(CVIRQLevels level);
        CVIRQLevels     GetLevel(void);
        int             SetAM(CVAddressModifier am);
        CVAddressModifier GetAM(void);
        int             SetDatasize(CVDataWidth datasize);
        CVDataWidth     GetDataSize(void);
        int             SetBaseAddress(Data16 baseaddress);
        Data16          GetBaseAddress(void);
        void            CheckStatus(CVErrorCodes status) const;
        bool            CheckIRQ();
        void            SetPulse();
        void            SendBUSY(BusyLevel level);
};

1109

```

1110 A.3.4 Configuration file

Source Code A.6: INI configuration file template for 4 TDCs. In section [**General**], the number of TDCs is explicated and information about the ongoing run is given. Then, there are sections for each and every VME modules. There buffer addresses are given and for the TDCs, the list of channels to enable is given. Finally, in section [**TDCSettings**], a part of the TDC settings are given.


```
[General]
TdcS=4
ScanID=$scanid
HV=$HV
RunType=$runtype
MaxTriggers=$maxtriggers
Beam=$beam
[VMEInterface]
Type=V1718
BaseAddress=0xFF0000
Name=VmeInterface
[TDC0]
Type=V1190A
BaseAddress=0x00000000
Name=Tdc0
StatusA00-15=1
StatusA16-31=1
StatusB00-15=1
StatusB16-31=1
StatusC00-15=1
StatusC16-31=1
StatusD00-15=1
StatusD16-31=1
[TDC1]
Type=V1190A
BaseAddress=0x11110000
Name=Tdc1
StatusA00-15=1
StatusA16-31=1
StatusB00-15=1
StatusB16-31=1
StatusC00-15=1
StatusC16-31=1
StatusD00-15=1
StatusD16-31=1
1112 [TDC2]
Type=V1190A
BaseAddress=0x22220000
Name=Tdc2
StatusA00-15=1
StatusA16-31=1
StatusB00-15=1
StatusB16-31=1
StatusC00-15=1
StatusC16-31=1
StatusD00-15=1
StatusD16-31=1
[TDC3]
Type=V1190A
BaseAddress=0x44440000
Name=Tdc3
StatusA00-15=1
StatusA16-31=1
StatusB00-15=1
StatusB16-31=1
StatusC00-15=1
StatusC16-31=1
StatusD00-15=1
StatusD16-31=1
[TDCSettings]
TriggerExtraSearchMargin=0
TriggerRejectMargin=0
TriggerTimeSubtraction=0b1
TdcDetectionMode=0b01
TdcResolution=0b10
TdcDeadTime=0b00
TdcHeadTrailer=0b1
TdcEventSize=0b1001
TdcTestMode=0b0
BLTMode=1
```

1113 **A.3.5 DAQ algorithm overview**

1114 **A.4 Software export**

B

1115

1116 Details on the online analysis package

1117 **B.1 Introduction**

1118 insert text here

C

1119

1120

1121

Structure of the hybrid simulation software

1122 C.1 Introduction

1123 insert text here...

